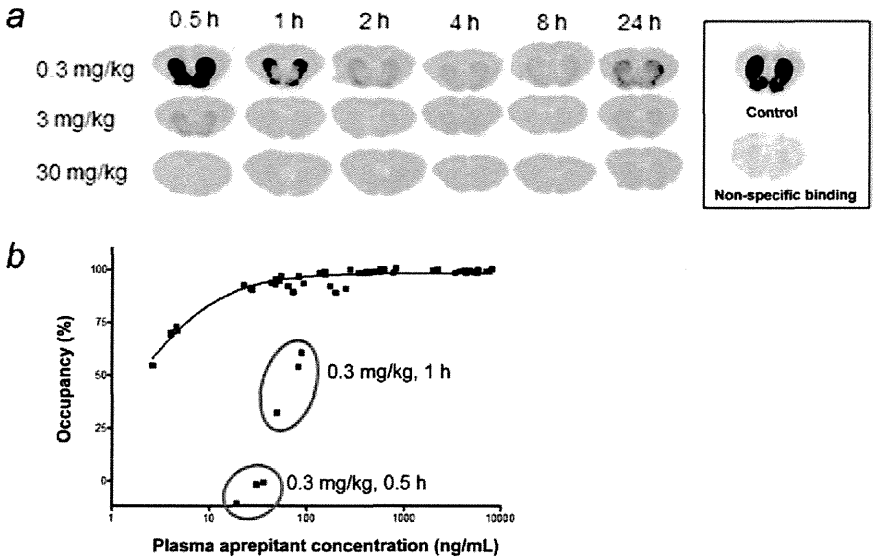

Figure 5. *Ex vivo* analysis of NK-1 receptor occupancy by aprepitant in the gerbil striatum at different time points after oral administration. (A) Representative autoradiograms showing binding of [^{18}F]FE-SPA-RQ to coronal sections of gerbil brains containing the striatum at 0.5, 1, 2, 4, 8, and 24 h (left to right) after aprepitant administration at doses of 0.3, 3, and 30 mg/kg (top to bottom). Radiolabeling of sections from untreated gerbils without (control) and with 10 μM aprepitant (non-specific binding) are displayed in the far right panel. (B) Striatal NK-1 receptor occupancy by aprepitant plotted against plasma concentrations of aprepitant in gerbils. The regression curve was generated as in the PET assays, and outlier data (indicated by circles), presumably in a non-equilibrium state, were excluded from the model fit.

Table 2. Striatal NK-1 receptor occupancy by aprepitant and plasma aprepitant concentrations in gerbils after oral aprepitant administration

		Time after administration					
		0.5 h	1 h	2 h	4 h	8 h	24 h
Parameter	Dose	(n = 3)	(n = 3)	(n = 3)	(n = 3)	(n = 3)	(n = 5)
Occupancy (%)	0.3 mg/kg	-4.54±3.10	48.8±8.60	91.4±1.20	95.2±0.72	93.0±0.34	67.5±3.31
	3 mg/kg	90.6±0.84	98.7±0.21	99.3±0.32	99.0±0.71	99.2±0.26	93.5±1.19
	30 mg/kg	99.6±0.08	99.1±0.20	99.3±0.52	99.2±0.44	98.9±0.29	98.6±0.33
Plasma Concentration (ng/mL)	0.3 mg/kg	28.5±5.0	72.6±11.9	75.6±8.3	61.4±10.2	37.3±7.6	4.0±0.4
	3 mg/kg	205.7±23.1	453.4±18.4	569.6±7.9	649.8±140.1	476.1±69.5	40.5±5.7
	30 mg/kg	2070.7±67.9	4438.0±441.9	6883.4±702.4	4949.7±409.7	4061.7±392.7	209.5±40.4

Data are expressed as mean ± SE.

Discussion

The present study demonstrated the validity of [^{18}F]FE-SPA-RQ-PET in small animals for estimating the pharmacodynamics measures of central NK-1 receptor occupancy by aprepitant and their relationships to its plasma pharmacokinetics.

Due to the relatively slow kinetics of [^{18}F]FE-SPA-RQ, we performed dynamic PET data acquisition in gerbils over 360 min after radioligand injection, but our time-stability analyses also indicated that the duration for a dynamic scan could be shortened to 120 min (Figure 3A). Quantification of specific radioligand binding could be made even shorter by conducting a 15 min static PET scan at 120 min after radioligand injection (Figure 3B and C), resulting in an increase of analytical throughput. By serially scanning gerbils with this method and by placing two animals on the stage of a PET scanner, data would be obtainable from 10 gerbils or more after a single radiosynthesis.

PET results in gerbils also suggested caution regarding the measurement of striatal NK-1 receptor occupancies, as the retention of [^{18}F]FE-SPA-RQ was not reduced to a level equivalent to the cerebellum even with an excessive dose of aprepitant. This is attributable to the strong accumulation of [^{18}F]FE-SPA-RQ in the Harderian glands and the consequent spillover of radioactivity to the anterior striatum. Such spillover is also likely to hamper precise determination of receptor occupancies induced by low-concentration aprepitant (Figure 4), although inclusion and exclusion of these data sets did not critically affect the result of the curve fit. Despite these technical issues, a fairly reasonable EC_{50} value (5.5 ng/mL) was obtained by assuming that aprepitant occupied 50% of total NK-1 receptors when reduction of specific radioligand binding was 50% of the maximal blockade. Indeed, EC_{50} of aprepitant in humans was approximately 10 ng/mL (Bergström et al., 2004). The proportion of protein-bound aprepitant in plasma is relatively high, and fractions of protein-unbound aprepitant in gerbil and human plasma were 0.36% and 0.7%, respectively. The EC_{50} value in gerbils, corrected for this species difference in protein binding, is 10.5 ng/mL, and is in good agreement with the actual measure in humans.

It was reported that 90% and 95% occupancies of striatal NK-1 receptors by aprepitant were required for therapeutic efficacies in treatments of vomiting and overactive bladder, respectively (Bergström et al., 2004; Green et al., 2006). In a manner

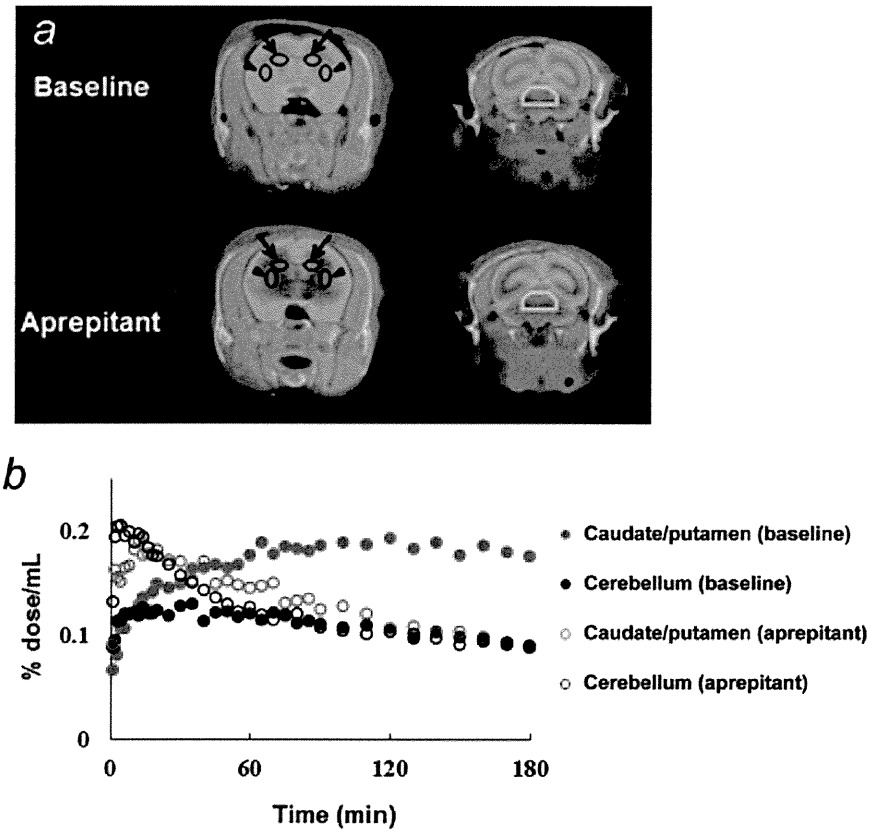

Figure 6. *In vivo* distribution of [^{18}F]FE-SPA-RQ in the marmoset brain. (A) Coronal PET images containing the caudate/putamen (left) and cerebellum (right) at baseline (top) and after oral aprepitant administration at a dose of 20 mg/kg (bottom). PET images were generated by averaging dynamic data from 0–180 min after intravenous radioligand injection and overlaid on the MRI template. ROIs were placed on the caudate (arrows), putamen (arrowheads), and cerebellum (cyan lines). (B) Time–activity curves for [^{18}F]FE-SPA-RQ in the caudate/putamen (red symbols) and cerebellum (black symbols) of the marmoset at baseline (closed symbols) and after aprepitant administration (open symbols). Radioligand uptake into each region was expressed as a percentage of the injected dose per unit tissue volume (%dose/mL).

similar to EC_{50} determination, EC_{90} and EC_{95} in the striatum of gerbils were estimated to be 50 and 105 ng/mL, respectively. These values could be translated to be 94 and 199 ng/mL after correction for the species difference in plasma protein binding of aprepitant, which were comparable to EC_{90} (~100 ng/mL) and EC_{95} (~190 ng/mL), as reported elsewhere (Bergström et al., 2004), supporting the feasibility of using gerbil PET data for acquiring preliminary indices toward prediction of clinically-optimal doses of aprepitant.

To circumvent the interference in brain quantitation due to spillover from Harderian glands, we conducted *ex vivo* studies using brain slices obtained from aprepitant-treated gerbils. In contrast to *in vivo* PET, *ex vivo* autoradiography indicated nearly 100% receptor occupancy by high-dose aprepitant. Our data also showed that NK-1 receptor occupancy by aprepitant was rather stationary at 4–8 h after oral administration, justifying PET assays initiated at 4 h. Meanwhile, receptor occupancies at 0.5 and 1 h after administration of low-dose (0.3 mg/kg) aprepitant could not be described by a direct model linking pharmacokinetic and pharmacodynamic parameters, presumably due to the lack of a pseudo-equilibrium between plasma and brain compartments. EC_{90} and EC_{95}, calculated by applying Hill's plot to the observed data after eliminating these outliers, were 16 and 34 ng/mL, respectively. These values were comparable to, but slightly smaller than the *in vivo* PET estimates. This small discrepancy might arise from inclusion of *ex vivo* data at 24 h, which may not follow a pseudo-equilibrium model. In fact, dissociation between brain and plasma aprepitant concentrations was documented previously (Lindström et al., 2007), implying a notable hysteresis in the relationship between plasma pharmacokinetics and brain pharmacodynamics. Hence, *ex vivo* EC_{90} and EC_{95} values would become even closer to the *in vivo* measures by adding data in a pseudo-equilibrium state (e.g., samples at 4–8 h after administration of aprepitant at doses <0.3 mg/kg).

A full blockade of specific radioligand binding in the striatum, without critical influences of extracranial radioactive signals, was demonstrated by a PET scan of a common marmoset treated with high-dose aprepitant, providing additional proof of the effects of radioactive spillover from the Harderian glands in gerbils. Dynamic PET data in the marmoset also suggested that a steady state of radioligand binding could not be pursued by PET imaging over 180 min. Indeed, BP_{ND} values were not time-stable in this scanning method (data not shown). Therefore, PET analyses over a long period would be needed to determine the minimal dynamic imaging time for quantifying binding potentials and to seek an appropriate time frame for a simplified, ratio-based estimation of radioligand binding. This would eventually allow a static PET scan protocol for marmosets with a reasonably high throughput.

A practical strategy for the characterization of aprepitant using small-animal PET can be proposed on the basis of the current findings. [^{18}F]FE-SPA-RQ-PET scans in gerbils could be carried out at multiple time points after treatment with aprepitant at different doses to efficiently outline the pharmacodynamics profiles of aprepitant in the brain and their relationship to its plasma pharmacokinetics. PET imaging of marmosets with [^{18}F]

FE-SPA-RQ could subsequently be conducted at selected time points suitable for a direct model fit to more precisely determine links between the pharmacokinetics and pharmacodynamics of aprepitant in a pseudo-equilibrium state. This workflow would also enable the characterization of new drug candidates that act on central NK-1 receptors, and would possibly facilitate a prediction of its effective plasma concentration in humans. While slow kinetics of aprepitant in the brain could be captured with [^{18}F]SPA-RQ and [^{18}F]FE-SPA-RQ, which also exhibit relatively slow kinetics (Hietala et al., 2005; Okumura et al., 2008), new PET ligands with rapid dissociation from binding sites and clearance from the brain would be required for evaluations of novel NK-1 receptor antagonists with faster kinetics.

Acknowledgments

The authors are grateful to Hiroshi Mizuuchi, Yukiko Shoji, Toru Watanabe, Masaki Yamada, and Masami Takahashi for their support of the analyses in this study. We also thank Takeharu Minamihisamatsu and the staff of the Molecular Probe Program for technical assistance and production of radioisotopes.

Statement of Interest

The authors declare no competing financial interests.

References

Aosaki T, Kawaguchi (1996) Actions of substance P on rat neostriatal neurons in vitro. J Neurosci 16:5141–5153.

Bergstrom M, Hargreaves RJ, Burns HD, Goldberg MR, Sciberras D, Reines SA, Petty KJ, Ogren M, Antoni G, Langstrom B, Eskola O, Scheinin M, Solin O, Majumdar AK, Constanzer ML, Battisti WP, Bradstreet TE, Gargano C, Hietala J (2004) Human positron emission tomography studies of brain neurokinin 1 receptor occupancy by aprepitant. Biol Psychiatry 55:1007–1012.

Blomeley CP, Kehoe LA, Bracci E (2009) Substance P mediates excitatory interactions between striatal projection neurons. J Neurosci 29:4953–4963.

Fong TM, Yu H, Strader CD (1992) Molecular basis for the species selectivity of the neurokinin-1 receptor antagonists CP-96,345 and RP67580. J Biol Chem 267:25668–25671.

George DT, Gilman J, Hersh J, Thorsell A, Herion D, Geyer C, Peng X, Kielbasa W, Rawlings R, Brandt JE, Gehlert DR, Tauscher JT, Hunt SP, Hommer D, Heilig M (2008) Neurokinin 1 receptor antagonism as a possible therapy for alcoholism. Science 319:1536–1539.

Green SA, Alon A, Ianus J, McNaughton KS, Tozzi CA, Reiss TF (2006) Efficacy and safety of a neurokinin-1 receptor antagonist in postmenopausal women with overactive bladder with urge urinary incontinence. J Urol 176:2535–2540.

Hamill T, Ryan C, Krause S, Eng W, Sanabria S, Francis B, Hargreaves R, Burns D (2003) The synthesis and in vivo characterization of [^{18}F] FESPARQ, a neurokinin-1 (NK1) receptor PET ligand. J Labelled Comp Radiopharm 46:S35–S35.

Haneda E, Higuchi M, Maeda J, Inaji M, Okauchi T, Ando K, Obayashi S, Nagai Y, Narazaki M, Ikehira H (2007) In vivo mapping of substance P receptors in brains of laboratory animals by high-resolution imaging systems. Synapse 61:205–215.

Hayashi M (1992) Ontogeny of some neuropeptides in the primate brain. Prog Neurobiol 38:231–260.

Hietala J, Nyman M, Eskola O, Laakso A, Grönroos T, Oikonen V, Bergman J, Haaparanta M, Forsback S, Marjamäki P, Lehikoinen P, Goldberg M, Burns D, Hamill T, Eng W-S, Coimbra A, Hargreaves R, Solin O (2005) Visualization and quantification of neurokinin-1 (NK1) receptors in the human brain. Mol Imaging Biol 7:262–272.

Jakab RL, Hazrati LN, Goldman RP (1996) Distribution and neurochemical character of substance P receptor (SPR)-immunoreactive striatal neurons of the macaque monkey: accumlation of SP fibers and SPR neurons and dendrites in 'striocapsules' encircling striosomes. J Comp Neurol 411:137–149.

Keller M, Montgomery S, Ball W, Morrison M, Snavely D, Liu G, Hargreaves R, Hietala J, Lines C, Beebe K, Reines S (2006) Lack of efficacy of the substance p (neurokinin1 receptor) antagonist aprepitant in the treatment of major depressive disorder. Biol Psychiatry 59:216–223.

Kincy-Cain T, Bost KL (1996) Increased susceptibility of mice to Salmonella infection following in vivo treatment with the substance P antagonist, spantide II. J Immunol 157:255–264.

Kramer MS, Winokur A, Kelsey J, Preskorn SH, Rothschild AJ, Snavely D, Ghosh K, Ball WA, Reines SA, Munjack D, Apter JT, Cunningham L, Kling M, Bari M, Getson A, Lee Y (2004) Demonstration of the efficacy and safety of a novel substance P (NK1) receptor antagonist in major depression. Neuropsychopharmacology 29:385–392

Kramer MS et al. (1998) Distinct mechanism for antidepressant activity by blockade of central substance P receptors. Science 281:1640–1645.

Lammertsma AA, Bench CJ, Hume SP, Osman S, Gunn K, Brooks DJ, Frackowiak RS (1996) Comparison of methods for analysis of clinical [11C]raclopride studies. J Cereb Blood Flow Metab 16:42–52.

Lecci A, Maggi CA (2001) Tachykinins as modulators of the micturition reflex in the central and peripheral nervous system. Regul Pept 101:1–18.

Lévesque M1, Wallman MJ, Parent R, Sík A, Parent A (2007) Neurokinin-1 and neurokinin-3 receptors in primate substantia nigra. Neurosci Res 57:362–371.

Lindstrom E, von Mentzer B, Pahlman I, Ahlstedt I, Uvebrant A, Kristensson E, Martinsson R, Noven A, de Verdier J, Vauquelin G (2007) Neurokinin 1 receptor antagonists: correlation between in vitro receptor interaction and in vivo efficacy. J Pharm Exp Ther 322:1286–1293.

McRitchie DA, Törk I (1994) Distribution of substance P-like immunoreactive neurons and terminals throughout the nucleus of the solitary tract in the human brainstem. J Comp Neurol 343:83–101.

Metwali A, Blum AM, Elliott DE, Setiawan T, Weinstock JV (2004) Cutting edge: hemokinin has substance P-like function and expression in inflammation. J Immunol 172:6528–6532.

Nakanishi S (1991) Mammalian tachykinin receptors. Annu Rev Neurosci 14:123–136.

Okumura M, Arakawa R, Ito H, Seki C, Takahashi H, Takano H, Haneda E, Nakao R, Suzuki H, Suzuki K, Okubo Y, Suhara T (2008) Quantitative analysis of NK1 receptor in the human brain using PET with ^{18}F-FE-SPA-RQ. J Nucl Med 49:1749–1755.

Otsuka M, Yoshioka K (1993) Neurotransmitter functions of mammalian tachykinins. Physiol Rev 73:229–308.

Reiner A, Hart NM, Lei W, Deng Y (2010) Corticostriatal projection neurons - dichotomous types and dichotomous functions. Front Neuroanat 4:142.

Ribeiro DS, Hökfelt T (2000) Neuroanatomical localisation of Substance P in the CNS and sensory neurons. Neuropeptides 34:256–271.

Rigby M, O'Donnell R, Rupniak NMJ (2005) Species differences in tachykinin receptor distribution: further evidence that the

substance P (NK1) receptor predominates in human brain. J Comp Neurol 490:335–353.

Rioux L, Joyce JN (1993) Substance P receptors are differentially affected in Parkinson's and Alzheimer's disease. J Neural Transm Park Dis Dement Sect 6:199–210.

Sanger GJ (2004) Neurokinin NK1 and NK3 receptors as targets for drugs to treat gastrointestinal motility disorders and pain. Br J Pharmacol 141:1303–1312.

Snider WD, McMahon SB (1998) Tackling pain at the source: new ideas about nociceptors. Neuron 20:629–632.

Tai YC, Ruangma A, Rowland D, Siegel S, Newport DF, Chow PL, Laforest R (2005) Performance evaluation of the microPET focus: a third-generation microPET scanner dedicated to animal imaging. J Nucl Med 46:455–463.

Tattersall FD, Rycroft W, Cumberbatch M, Mason G, Tye S, Williamson DJ, Hale JJ, Mills SG, Finke PE, MacCoss M, Sadowski S, Ber E, Cascieri M, Hill RG, MacIntyre DE, Hargreaves RJ (2000) The novel NK1 receptor antagonist MK-0869 (L-754,030) and its water soluble phosphoryl prodrug, L-758,298, inhibit acute and delayed cisplatin-induced emesis in ferrets. Neuropharmacology 39:652–663.

Tooney P, Crawter V, Chahl L. (2001) Increased tachykinin NK1 receptor immunoreactivity in the prefrontal cortex in schizophrenia. Biol Psychiatry 49:523–527.

Tooney P, Weidenhofer J, Yip J, Zavitsanou K, Huang XF, Chahl LA (2006) Immunohistochemical localisation of the NK1 receptor in the human amygdala: preliminary investigation in schizophrenia. Prog Neuropsychopharmacol Biol Psychiatry 30:1313–1321.

Yasuno F, Sanabria SM, Burns D, Hargreaves RJ, Ghose S, Ichise M, Chin FT, Morse CL, Pike VW, Innis RB (2007) PET imaging of neurokinin-1 receptors with [(^{18}F]SPA-RQ in human subjects: assessment of reference tissue models and their test-retest reproducibility. Synapse 61:242–251.

Zandbelt BB, van Buuren M, Kahn RS, Vink M (2011) Reduced proactive inhibition in schizophrenia is related to corticostriatal dysfunction and poor working memory. Biol Psychiatry 70:1151–1158.

Zhang MR, Maeda J, Furutsuka K, Yoshida Y, Ogawa M, Suhara T, Suzuki K (2003) [^{18}F]FMDAA1106 and [^{18}F]FEDAA1106: two positron-emitter labeled ligands for peripheral benzodiazepine receptor (PBR). Bioorg Med Chem Lett 13:201–204.

In Vivo SPECT Imaging of Amyloid-β Deposition with Radioiodinated Imidazo[1,2-*a*]Pyridine Derivative DRM106 in a Mouse Model of Alzheimer's Disease

Chun-Jen Chen[1–3], Kazunori Bando[1], Hiroki Ashino[1], Kazumi Taguchi[1], Hideaki Shiraishi[1], Keiji Shima[1], Osuke Fujimoto[1], Chiemi Kitamura[1], Satoshi Matsushima[1], Keisuke Uchida[1], Yuto Nakahara[1], Hiroyuki Kasahara[1], Takao Minamizawa[1], Cheng Jiang[4], Ming-Rong Zhang[2], Maiko Ono[2], Masaki Tokunaga[2], Tetsuya Suhara[2], Makoto Higuchi[2], Kazutaka Yamada[3], and Bin Ji[2]

[1]Research Department, Fujifilm RI Pharma Co. LTD, Chiba, Japan; [2]Molecular Imaging Center, National Institute of Radiological Sciences, Chiba, Japan; [3]Clinical Veterinary Science, The United Graduate School of Veterinary Science, Gifu University, Gifu, Japan; and [4]School of Pharmacy, Fudan University, Shanghai, China

Noninvasive determination of amyloid-β peptide (Aβ) deposition has important significance for early diagnosis and medical intervention for Alzheimer's disease (AD). In the present study, we investigated the availability of radiolabeled DRM106 ($^{123/125}$I-DRM106 [6-iodo-2-[4-(1*H*-3-pyrazolyl)phenyl]imidazo[1,2-*a*]pyridine]), a compound with sufficient affinity for the synthesis of human Aβ fibrils and satisfactory metabolic stability, as a SPECT ligand in living brains. **Method:** The sensitivity of ^{125}I-DRM106 for detecting Aβ deposition was compared with that of ^{125}I-IMPY (2-(4′-dimethylaminophenyl)-6-iodo-imidazo[1,2-a]pyridine), a well-known amyloid SPECT ligand, by ex vivo autoradiographic analyses in 18-mo-old amyloid precursor protein transgenic mice. To verify the sensitivity and quantitation of radiolabeled DRM106 for in vivo imaging, we compared the detectability of Aβ plaques with ^{123}I-DRM106 and a well-known amyloid PET agent, ^{11}C-labeled Pittsburgh compound B (^{11}C-PiB), in 29-mo-old transgenic mice and age-matched nontransgenic littermates. Additionally, we compared the binding characteristics of ^{125}I-DRM106 with those of ^{11}C-PiB and ^{11}C-PBB3, which selectively bind to Aβ plaques and preferentially to tau aggregates, respectively, in postmortem AD brain sections. **Results:** Ex vivo autoradiographic analysis showed that measurement with ^{125}I-DRM106 has a higher sensitivity for detecting Aβ accumulation than with ^{125}I-IMPY in transgenic mice. SPECT imaging with ^{123}I-DRM106 also successfully detected Aβ deposition in living aged transgenic mice and showed strong correlation ($R = 0.95$, $P < 0.01$) in quantitative analysis for Aβ plaque detection by PET imaging with ^{11}C-PiB, implying that sensitivity and quantitation of SPECT imaging with ^{123}I-DRM106 are almost as good as ^{11}C-PiB PET for the detectability of Aβ deposition. Further, the addition of nonradiolabeled DRM106 fully blocked the binding of ^{125}I-DRM106 and ^{11}C-PiB, but not ^{11}C-PBB3, to AD brain sections, and ^{125}I-DRM106 showed a lower binding ratio of the diffuse plaque–rich lateral temporal cortex to the dense-cored/neuritic plaque–rich hippocampal CA1 area, compared with ^{11}C-PiB. **Conclusion:** All of these data demonstrated the high potential of ^{123}I-DRM106 for amyloid imaging in preclinical and clinical application, and it might more preferentially detect dense-cored/neuritic amyloid deposition, which is expected to be closely associated with neuropathologic changes of AD.

Key Words: Alzheimer's disease (AD); amyloid imaging; amyloid precursor protein (APP) transgenic mouse; DRM106; single photon emission computed tomography (SPECT)

J Nucl Med 2015; 56:120–126
DOI: 10.2967/jnumed.114.146944

Alzheimer's disease (AD) is a progressive neurodegenerative disorder characterized by 2 pathologic hallmarks: amyloid-β peptide (Aβ) plaques and neurofibrillary tangles (NFTs). In vivo noninvasive detection of Aβ deposition is important for early diagnosis and medical intervention of AD at a prodromal stage, because fibrillary Aβ has already been accumulating in the brain for a few decades before AD onset (*1*). Molecular imaging with nuclear medicine technologies such as PET and SPECT is available for both preclinical and clinical use and is considered as a bridge between them. Over the past few years, the availabilities of several PET tracers for amyloid imaging have been successfully verified in AD patients. ^{11}C-labeled Pittsburgh compound B (^{11}C-PiB) is the most widely used PET ligand with which investigators have assessed the longitudinal, quantitative Aβ accumulation in AD model mice and patients (*2–4*) and verified amyloid deposition as a useful imaging biomarker for AD diagnosis, prognostic judgment for conversion from mild cognitive impairment to AD, and evaluation for antiamyloid therapies (*5–7*). To overcome the shortcoming of the limited half-life (~20 min) of ^{11}C-labeled tracers, ligands labeled with ^{18}F (half-life, ~110 min) have also been developed for further routine medical needs (*8–11*).

Although inferior to PET in terms of sensitivity and quantitative performance, SPECT imaging has advantages of operating cost and already-installed rate in medical hospitals, making it more suitable for primary screening for prodromal AD patients. For the past decade, several SPECT ligands have been developed for amyloid imaging. ^{123}I-IMPY (2-(4′-dimethylaminophenyl)-6-iodo-imidazo[1,2-a]pyridine) is a SPECT tracer with high affinity for Aβ fibrils, and in vitro autoradiographic analysis has successfully detected amyloid deposition on brain sections from both AD models

Received Aug. 11, 2014; revision accepted Nov. 3, 2014.
For correspondence or reprints contact: Bin Ji, Molecular Imaging Center, National Institute of Radiological Sciences, 4-9-1, Anagawa, Inage-ku, Chiba-shi, Chiba 263-8555, Japan.
E-mail: kihin@nirs.go.jp
Published online Dec. 4, 2014.

and AD patients (*12–16*). However, preliminary clinical data for ^{123}I-IMPY showed a poor signal-to-noise ratio, making it difficult to distinguish between cognitively normal persons and AD patients, possibly because of insufficient affinity for Aβ fibrils, poor brain permeability, or metabolic instability (*17*). Recently, we developed a series of imidazopyridine compounds for amyloid SPECT imaging and obtained a promising candidate compound, termed DRM106 (6-iodo-2-[4-(1*H*-3-pyrazolyl)phenyl]imidazo[1,2-*a*]pyridine), which has higher affinity for synthetic human Aβ fibrils and metabolic stability. In vitro autoradiography with ^{125}I-labeled DRM106 also successfully detected Aβ plaques in postmortem AD patient brains (*18*). In the present study, we performed in vivo imaging with this newly developed SPECT ligand in living model mice with AD-like amyloid pathology and compared it with ^{11}C-PiB in the detectability of Aβ deposition.

MATERIALS AND METHODS

Radiosynthesis of Radioligands

The radiosynthesis of ^{125}I-DRM106, ^{125}I-IMPY, ^{11}C-PiB, and ^{11}C-PBB3 (2-((1*E*,3*E*)-4-(6-(^{11}C-methylamino)pyridin-3-yl)buta-1,3-dienyl)benzo[*d*]thiazol-6-ol) was performed as described in previous publications (*2,12,18,19*). The radiochemical purity of ^{125}I-DRM106, ^{125}I-IMPY, ^{11}C-PiB, and ^{11}C-PBB3 was greater than 95%, and specific radioactivity was 81.4, 81.4, 93–354, and 72–204 GBq/μmol, respectively, at the end of synthesis.

^{123}I-DRM106 was prepared by the reaction of its precursor with ^{123}I-NaI in the presence of chloramine T (Fig. 1). Briefly, chloramine T (0.035 mg/20 μL 2-propanol) was added to 4.5 mL of 35 mM phosphate buffer (pH 6.3) containing ^{123}I-NaI (29.9 GBq; Fujifilm RI Pharma Co., Ltd. [specific activity was adjusted to 714 GBq/μmol by addition of nonradiolabeled NaI]) and precursor (0.638 mg) and incubated for 5 min at room temperature, followed by quenching by the addition of 200 μL of 1N NaOH. Then the reaction mixture was incubated at 70°C for 30 min and terminated by cooling. The subsequent experimental procedure was the same, with the preparation of ^{125}I-DRM106 as described in our previous publication (*18*). The radiolabeling efficiency of ^{123}I-DRM106 was 65%–80% based on radio–thin-layer chromatography measurement. The radiochemical purity was greater than 95% at the end of synthesis, and the theoretic value of the specific activity was 714 GBq/μmol, considering that the reaction of ^{123}I-NaI and precursor led to the formation of ^{123}I-DRM106 with a 1:1 stoichiometric ratio.

Experimental Animals

A transgenic mouse line (Tg2576), which overexpresses a mutant form of amyloid precursor protein (APPK670/671 L), was purchased from Taconic Farms Inc. Then we generated a JU-Tg2576 mouse by backcrossing of Tg2576 with a JU strain (JU/Ct-C, A.) mouse over 29 generations under license agreement of the Mayo Foundation for Medical Education and Research from Daiichi Sankyo Co. Ltd. for easier daily handling. Transgenic mice (termed JU-Tg2576 if without special description) and body weight–matched nontransgenic JU strain mice as control animals were used in the present study, except for in vivo SPECT imaging, for which commercially available Tg2576 mouse brain was used.

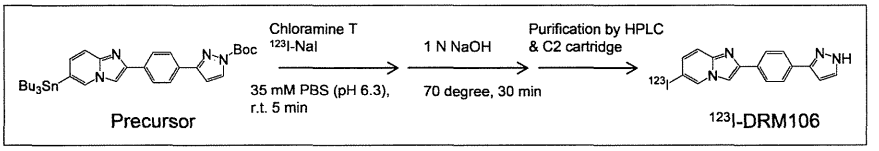

FIGURE 1. Radiosynthesis for ^{123}I-DRM106.

Preparation of Brain Homogenates and Aβ Fibrils, In Vitro Binding Assay and Aβ Assessment, In Vitro and Ex Vivo Autoradiographic Analysis and Metabolite Analysis, and Small-Animal PET and SPECT Imaging

Experimental procedures are presented in the supplemental data (supplemental materials are available at http://jnm.snmjournals.org).

Statistical Analysis

All statistical examinations in the present study were performed by SPSS software (SPSS Inc.). Statistical analyses for group comparisons were performed by Student *t* test or ANOVA followed by Bonferroni post hoc test. The correlation between 2 parameters was examined by parametric test with Pearson product-moment correlation coefficient (R). The difference between groups was considered significant at a *P* value less than 0.05. All data were expressed as mean ± SD.

RESULTS

In Vitro Binding of DRM106

Saturation curves and Scatchard analyses using a 2-site binding model demonstrated that the dissociation constant (K_d) values of high-affinity binding sites of DRM106 to synthetic human Aβ(1–40) and Aβ(1–42) fibrils, brain homogenates of transgenic mice, and AD patients were approximately 1–10 nM, and the K_d values of low-affinity sites were approximately 100–300 nM (Supplemental Fig. 1; Table 1). To estimate the correlation between quantitative ^{125}I-DRM106 binding and Aβ amounts, brain homogenates of transgenic mice at different ages (8.1–17 mo) were used for the measurement of ^{125}I-DRM106 binding and Aβ amounts. Age-dependent increases in ^{125}I-DRM106 binding and Aβ amounts were detected, and there was excellent correlation between ^{125}I-DRM106 binding and the amount of either Aβ(1–40) ($R = 1$, $P < 0.01$) or Aβ(1–42) ($R = 0.99$, $P < 0.01$) (Fig. 2).

Metabolite Analysis in Transgenic Mice

Solutions of ^{125}I-DRM106 (1.1 MBq) were injected into male JU-Tg2576 transgenic mice (age, 18 mo) via the tail vein, and metabolite analyses were performed as described in our previous publication (*18*). Similar to results in normal rats (*18*), there were no detectable metabolites in the brain over the observation period, whereas only a little metabolite-related radioactivity was observable in the plasma samples, in addition to unchanged ^{125}I-DRM106 (Fig. 3).

Ex Vivo Autoradiography with ^{125}I-DRM106 and ^{125}I-IMPY

The sensitivity of ^{125}I-DRM106 for detecting Aβ plaques was higher than that of ^{125}I-IMPY, based on the experimental observation that more amyloid plaques were detectable using ^{125}I-DRM106 than ^{125}I-IMPY at 3 indicated time points in 18-mo-old transgenic mice (Fig. 4). Meanwhile, no overt difference in amyloid deposition labeled by congo red was detectable between 2 experimental groups for ^{125}I-DRM106 and ^{125}I-IMPY analysis (data not shown). Although slight nonspecific binding of ^{125}I-DRM106 to white matter was detectable in both transgenic and nontransgenic mice at 1 h after injection, background radioactivity decreased to an undetectable level after 2 h (Fig. 4A), suggesting that the optimum scan time for in vivo imaging with radiolabeled DRM106 was between 1 and 2 h for acquiring good contrast with minimum loss in radioactive signals. Ex vivo emulsion autoradiography and consequent fluorescent labeling with thioflavin-S showed great consistency of ^{125}I-DRM106

TABLE 1
Binding Parameters of ^{125}I-DRM106

Sample	High-affinity binding site			Low-affinity binding site		
	K_d*	B_{max}†	BP‡	K_d	B_{max}	BP
Aβ(1–40) fibrils (n = 4)	1.50 ± 0.00	4.30 ± 1.00	—	1,400 ± 36.6	163 ± 9.60	—
Aβ(1–42) fibrils (n = 4)	10.1 ± 5.10	34.3 ± 22.8	—	2,890 ± 344.5	339 ± 268	—
Transgenic brain (n = 4)	4.20 ± 0.92	113 ± 133	26.9	264 ± 160	3,780 ± 1,008	14.3
AD brain	4.30 ± 1.20	681 ± 305	158.4	101 ± 37.8	7,050 ± 1,985	69.8

*K_d is expressed as nmol/L.
†B_{max} for Aβ fibrils and mouse/human tissues is expressed as pmol/nmol of Aβ and pmol/g of tissue.
‡BP = B_{max}/K_d.
Data of Aβ fibrils were from 4 independent experiments, and each experiment was run in triplicate. Data of transgenic brains were from 4 mice (20 mo old), and each experiment was run in triplicate. Data of AD brain were from triplicate experiments. Data are mean ± SD.
B_{max} = maximum binding value; mo = month.

accumulation and thioflavin-S–positive Aβ deposition (Supplemental Fig. 2).

In Vivo Imaging with ^{123}I-DRM106 SPECT and ^{11}C-PiB PET

To investigate the capacity of ^{123}I-DRM106 for in vivo detection of amyloid deposition, we performed in vivo imaging with ^{123}I-DRM106 and ^{11}C-PiB in the same mice and compared their quantitative analysis. The accumulation of ^{11}C-PiB in the frontal/parietal cortex and hippocampus regions enriched with amyloid deposition was more abundant than that in other brain regions in transgenic mice (Tg2576), whereas no regional difference in radioactivity accumulation was detectable in age-matched nontransgenic mice. In vivo images of ^{123}I-DRM106 showed great similarity to those of ^{11}C-PiB except for more intelligible accumulation in the cerebellum (Fig. 5A; Supplemental Fig. 3). Subsequent ex vivo autoradiography also clearly demonstrated consistency in radioligand accumulation with the observation of in vivo imaging. Quantitative analysis showed that both ^{11}C-PiB and ^{123}I-DRM106 accumulations in amyloid pathology–enriched regions (cortex/hippocampus) in transgenic mice were significantly higher than in nontransgenic mice (Fig. 5B). Positive correlations between amyloid depositions detected by these 2 radioligands (R = 0.95, $P < 0.01$) and between in vivo and ex vivo binding of ^{123}I-DRM106 (R = 0.98, $P < 0.01$) were statistically significant (Fig. 5C). Although using cerebellum with slight to moderate amyloid pathology as reference tissue would underestimate the binding potential (BP) calculated from the simplified reference tissue model, this would not affect our correlation analysis.

Binding of ^{125}I-DRM106, ^{11}C-PiB, and ^{11}C-PBB3 in Postmortem Human Brain

To evaluate binding sites of ^{125}I-DRM106 in AD brain, we compared the in vitro autoradiographic images of ^{125}I-DRM106 with ^{11}C-PiB or ^{11}C-PBB3, a radiolabeled ligand that binds to both amyloid and tau lesions at 5 nM of incubation concentration (*19*), in AD brain sections containing the hippocampus and lateral temporal cortex (LTCx) regions. The addition of nonradiolabeled DRM106 fully blocked the binding of ^{125}I-DRM106 and ^{11}C-PiB, and partially ^{11}C-PBB3, in AD brain sections (Fig. 6A). ^{125}I-DRM106, ^{11}C-PiB, and ^{11}C-PBB3 showed detectable specific binding in LTCx regions harboring numerous plaques including dense-cored/neuritic and diffuse plaques and NFTs, and in the hippocampal CA1 sector enriched with NFTs and Aβ deposition composed of numerous dense-cored/neuritic and few diffuse plaques, to greater or lesser degrees (Figs. 6B and 6C; Supplemental Fig. 4). The LTCx-to-CA1 ratio of ^{125}I-DRM106 binding was similar to that of ^{11}C-PBB3 but significantly lower than that of ^{11}C-PiB (Fig. 6D).

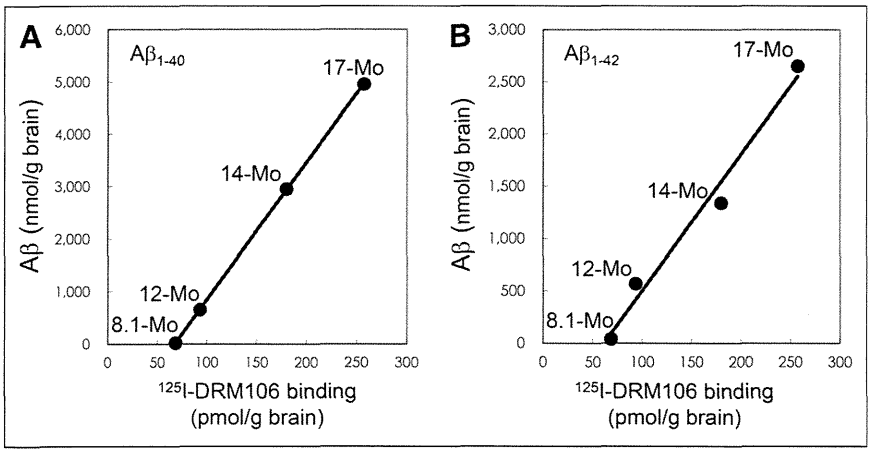

FIGURE 2. Correlation between amounts of Aβ species and binding of ^{125}I-DRM106. ^{125}I-DRM106 binding and amounts of Aβ were increased age-dependently in brain homogenates of transgenic mice at different ages as indicated, and correlations between ^{125}I-DRM106 binding and Aβ(1–40) (A) and Aβ(1–42) (B) amounts were statistically significant. Data were from average of triplicate experiments for each age group.

DISCUSSION

For development of a SPECT ligand for amyloid imaging, the compound IMPY is a good guide because it is the first SPECT imaging agent to be tested in human subjects, and a great deal of data have already been published for reference. In vitro autography with ^{123}I-IMPY clearly demonstrated its availability for visualization of Aβ plaques in either AD model (APP/PS1 double-transgenic mouse) or postmortem brain sections. Ex vivo autographic analysis also visually confirmed ^{123}I-IMPY–labeled Aβ plaques in aged APP/PS1 double-transgenic mice (*12*). The

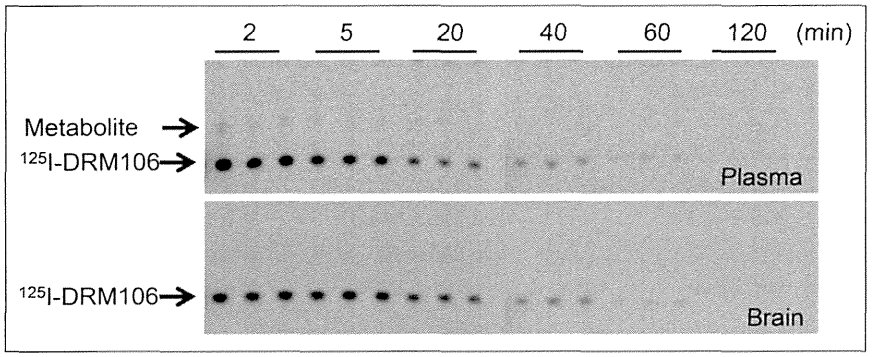

FIGURE 3. Metabolic stability of ^{125}I-DRM106 in transgenic mice. Plasma and brain samples were collected at indicated time points after intravenous injection of ^{125}I-DRM106. Thin-layer chromatography analysis clearly demonstrated that no overt metabolite in brain (lower) and only a little metabolite in plasma (upper) were detectable at the initial phase during observation period.

results of in vivo imaging with micro-SPECT, however, were not encouraging (*17*). Subsequent clinical studies also showed that the signal-to-noise ratio for plaque labeling was not as high as that of ^{11}C-PiB (*17*), indicating that successful development will require higher criteria as exemplified by higher metabolic stability and affinity for Aβ plaques than IMPY. The present and previous data clearly demonstrated that ^{125}I-DRM106 has satisfactory metabolic stability in rodents and higher affinity for synthetic human Aβ fibrils than IMPY (*18*). There was high-level specific binding of ^{123}I-DRM106 to Aβ deposition in Tg2576 mouse and postmortem AD patient brains with high affinity (K_d of 1-digit nM). This characteristic was similar to that of ^{11}C-PiB, as published in a previous study, at low nanomolar concentrations typically used in SPECT studies (*20*). Such improvements in the properties of imaging agents are responsible for the superiority of ^{125}I-DRM106 in the detectability of Aβ plaques, compared with ^{125}I-IMPY, as shown in ex vivo autoradiographic analysis (Fig. 4).

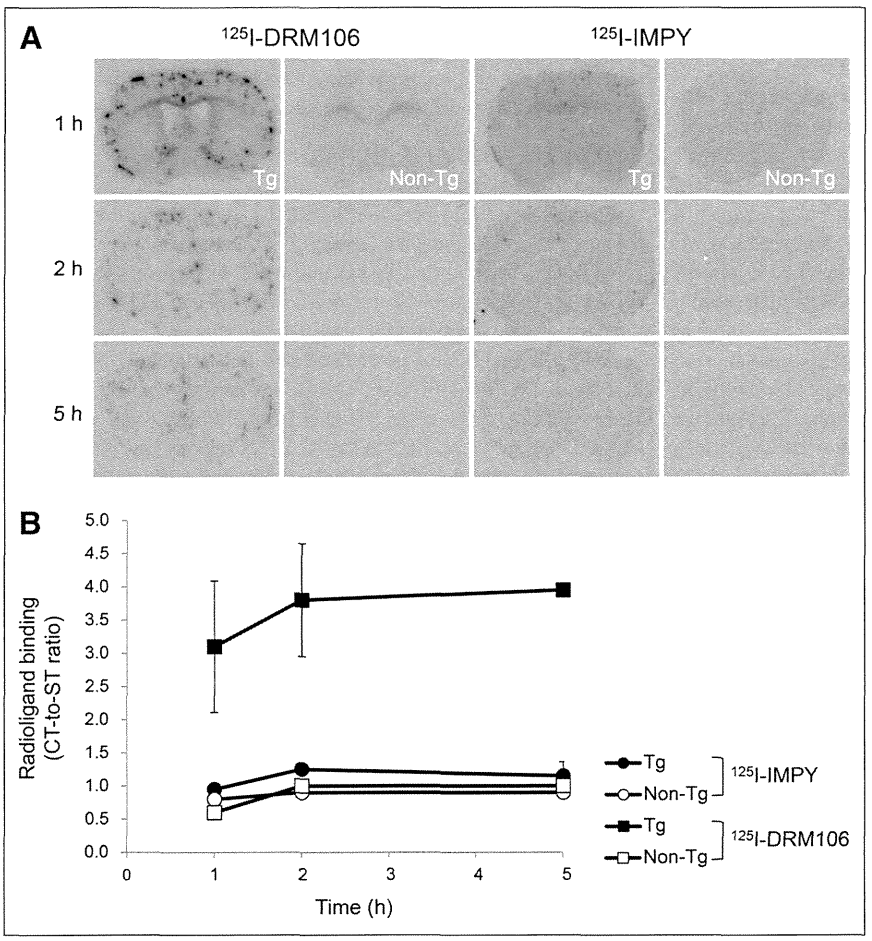

FIGURE 4. Ex autoradiographic analysis of ^{125}I-DRM106 and ^{125}I-IMPY in transgenic mouse brain. (A) Representative coronal images of 18-mo-old male transgenic (from left, first and third columns) and body weight–matched nontransgenic (from left, second and fourth columns) mice administered bolus injection of radiolabeled ^{125}I-DRM106 (from left, first and second columns) and ^{125}I-IMPY (from left, third and fourth columns) at 1, 2, and 5 h after injection. (B) Amyloidosis-associated accumulations of radioligands were quantified as ratios of radioactivity of neocortex to striatum. Data were from experiments shown in A. Transgenic (closed symbols, n = 2 for each time point) and nontransgenic (open symbols, n = 1 for each time point) mice were administered ^{125}I-DRM106 (squares) and ^{125}I-IMPY (circles). Data are mean ± SD. CT = neocortex; Non-Tg = nontransgenic; ST = striatum; Tg = transgenic.

Recently, amyloid deposition in 28-mo-old Tg2576 mice was successfully visualized with a radioiodine-labeled pyridyl benzofuran derivative (*21*). There was, however, relatively high retention, approximately 40% of initial brain uptake, in the normal brain even after 60 min and resulting high-level nonspecific binding to white matter (*21*). Given that white matter in human subjects is much more abundant than in rodents, such high-level nonspecific binding to white matter may overtly affect the detectability of Aβ plaques in human subjects. Additionally, this radioligand was not metabolically stable in normal mice. The intact form in plasma was decreased to approximately 20% at 30 min after injection (*21*), raising the undesirable possibility that these radioactive metabolites penetrated into the brain and lowered the signal-to-noise ratio. In contrast, the amount of ^{125}I-DRM106 remaining in the normal brain was lowered to less than 4% of initial uptake after 60 min, exhibiting excellent off-target washout (*18*). As a result, there was low nonspecific binding in white matter and other brain regions without amyloid pathology (Figs. 4 and 5). Additionally, a recent poster presentation—at the Alzheimer Association International Conference (*22*), during which a newly developed radioiodinated tracer, ^{123}I-ABC577, was reported—demonstrated the possible availability of image-based diagnosis for AD in human subjects. Although this is a preliminary result and there is still a lack of accurate information available, such as the chemical structure of ABC577, this successful case has proved the feasibility of this SPECT agent for amyloid imaging in human subjects.

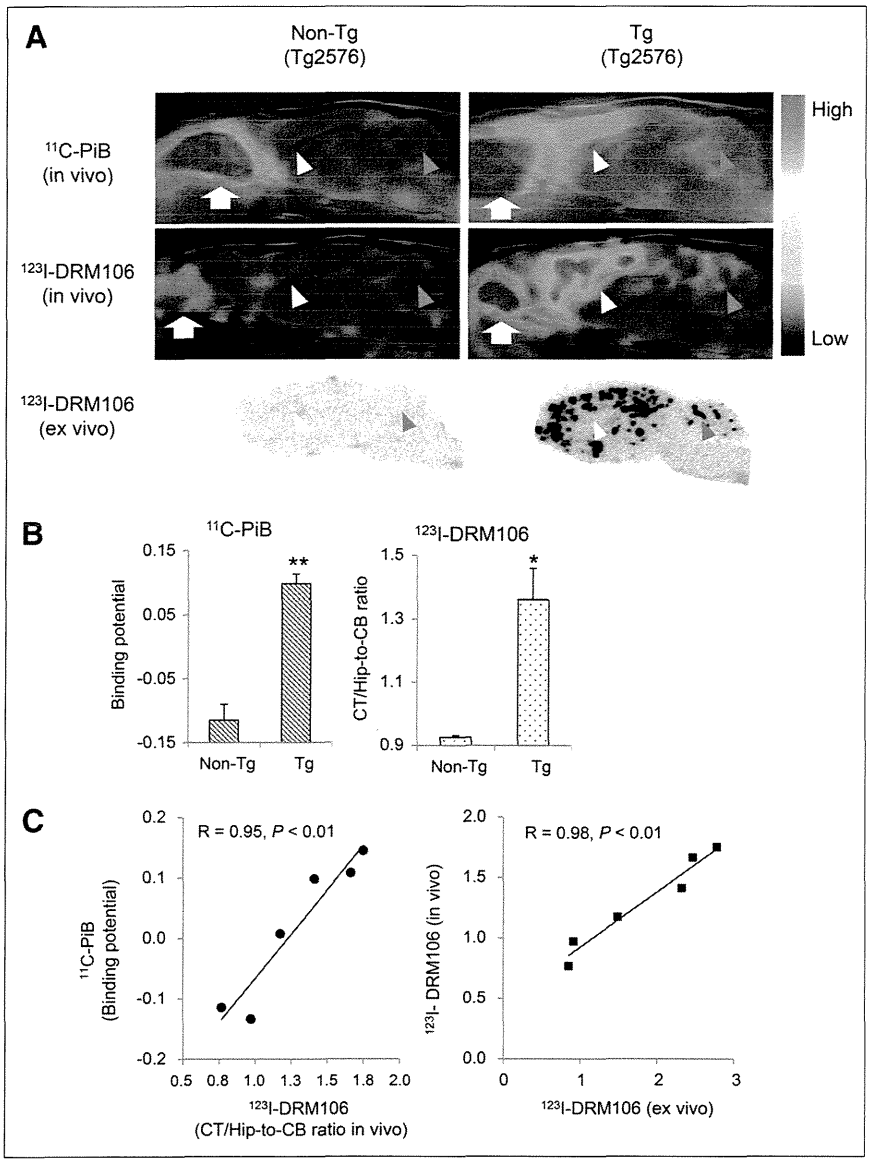

FIGURE 5. In vivo imaging with ^{123}I-DRM106 and ^{11}C-PiB. (A) Typical in vivo images of ^{11}C-PiB (top) and ^{123}I-DRM106 (middle) and ex vivo images of ^{123}I-DRM106 (bottom) in 28-mo-old female transgenic (Tg2576; right) and age-matched nontransgenic littermate (left) mouse brains. In vivo images were overlaid on MR imaging template. Red and yellow arrowheads indicate cerebellum and cortex/hippocampus regions, respectively. White arrows indicate harderian gland. (B) Quantitative analysis for in vivo binding of ^{11}C-PiB and ^{123}I-DRM106 in nontransgenic (n = 3) and transgenic (n = 5) mice. In vivo bindings of ^{11}C-PiB and ^{123}I-DRM106 were estimated by BP and cortex-to-cerebellum ratio, respectively. Data are mean ± SD. *P < 0.05 and **P < 0.01 vs. nontransgenic mouse, t test. (C) Correlation of in vivo binding between ^{11}C-PiB and ^{123}I-DRM106 (left) and between in vivo and ex vivo binding of ^{123}I-DRM106 (right). Data of mice that underwent both ^{11}C-PiB and ^{123}I-DRM106 scans were used for correlation analysis. Non-Tg = nontransgenic; Tg = transgenic.

In comparison with PET, radioisotopes used in SPECT, such as ^{123}I (half-life, 13.22 h), have a longer half-life and can therefore achieve longer distance delivery and cheaper operating cost, and more SPECT scanners have also been installed for routine clinical examinations, making it more suitable for primary screening for prodromal AD patients, especially in developing countries with large territories. Given that the sensitivity and quantitative ability of SPECT are inferior to those of PET, we need more in vivo imaging data to support the availability of DRM106 for further clinical application. We performed in vivo imaging with ^{123}I-DRM106 in Tg2576 mice and compared this with PET imaging with ^{11}C-PiB. Tg2576 is a widely used transgenic mouse line with AD-like amyloid pathology, with Aβ plaque density increasing exponentially from 12 mo, reaching levels similar to those seen in the AD brain (*23*). There were, however, many fewer amyloid-associated binding sites for ^{11}C-PiB in the Tg2576 mouse than in AD patient tissues (*2,24*). Despite the fewer binding sites for ^{11}C-PiB in Tg2576 mice, we successfully detected significant amyloid-associated ^{11}C-PiB accumulation in the living brains, taking advantage of the high-quality ^{11}C-PiB with high specific radioactivity up to approximately 300 GBq/umol, 6–10 times higher than the usually used level, and elderly mice (29 mo). Our comparative analysis showed great consistency in the quantitative detection of Aβ deposition between ^{123}I-DRM106 and ^{11}C-PiB, demonstrating that SPECT imaging with ^{123}I-DRM106 has quantitative ability and sensitivity similar to those of PET with ^{11}C-PiB in the living brain.

On the basis of our experimental result that the LTCx-to-CA1 ratio of binding of ^{125}I-DRM106 is significantly lower than that of ^{11}C-PiB, different pathologic aggregates are expected to provide major binding sites for ^{125}I-DRM106 and ^{11}C-PiB. Although the LTCx-to-CA1 ratio of binding of ^{125}I-DRM106 was similar to that of ^{11}C-PBB3, which binds to both Aβ and tau aggregates at the incubation concentration used (*19*), NFTs might not provide binding sites for ^{125}I-DRM106, because a high concentration of nonradiolabeled DRM106 failed to fully block the binding of ^{11}C-PBB3 when we postulated that NFTs provide similar binding sites for all of the β-sheet ligands. Thus, a reasonable explanation is that ^{125}I-DRM106 might preferentially bind to dense-cored/neuritic plaques as did other amyloid tracers such as ^{18}F-(fluorinated amyloid imaging compound of Tohoku University) (*25*). Given that ^{11}C-PiB also binds to diffuse plaques, in addition to dense-cored/neuritic plaques, the lower LTCx-to-CA1 ratio of binding of ^{125}I-DRM106 than ^{11}C-PiB is consistent with the distribution of Aβ plaques—that is, the major Aβ deposition is dense-cored/neuritic plaques in CA1. In contrast, in addition to dense-cored/neuritic plaques, numerous diffuse plaques are also observed in the LTCx region.

The correlation between PiB binding and the amounts of either Aβ(1–40) or Aβ(1–42) was not significant (*20*), being attributable to preferential binding of PiB to certain Aβ subtypes, such as $Aβ_{N3(pE)}$ (*2*). In contrast, ^{125}I-DRM106 binding showed excellent linearity with the amounts of either Aβ(1–40) or Aβ(1–42) in

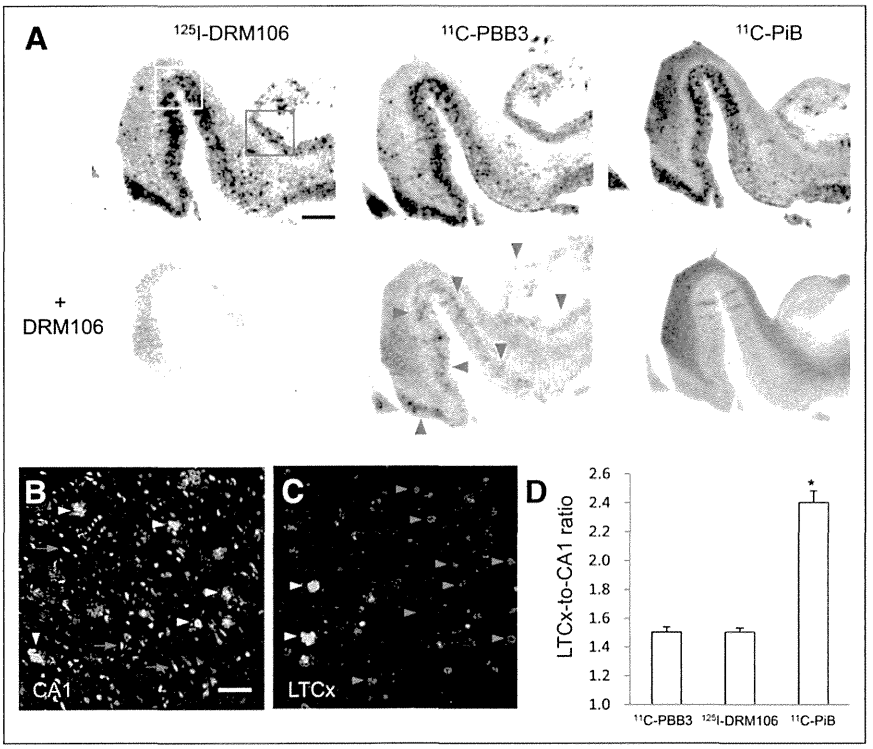

FIGURE 6. In vitro autoradiographic analyses with ^{125}I-DRM106, ^{11}C-PiB, and ^{11}C-PBB3 in postmortem AD brains. (A) Autoradiographic images of ^{125}I-DRM106 (left), ^{11}C-PBB3 (middle), and ^{11}C-PiB (right) and in absence (upper) or presence (lower) of nonradiolabeled DRM106 in brain sections from patient with AD. Slices contain hippocampus, parahippocampal gyrus, and fusiform gyrus. Areas outlined with white and red squares contain hippocampal CA1 and LTCx flanking collateral sulcus, respectively, and high-power images of these 2 regions are shown in Supplemental Fig. 4. Red arrowheads indicate putative NFT-associated binding of ^{11}C-PBB3. (B and C) Fluorescent counterstaining of NFTs (red arrows) and dense-cored/neuritic (yellow arrowheads) and diffuse (red arrowheads) plaques with FSB ((E,E)-1-fluoro-2,5-bis-(3-hydroxycarbonyl-4-hydroxy)styrylbenzene) in CA1 (B) and LTCx (C) regions. (D) Serial brain sections (5, 4, and 4 randomized sections for analyses of ^{125}I-DRM106, ^{11}C-PiB, and ^{11}C-PBB3, respectively) from patient with AD were used for quantitative analyses of specific bindings of these radiolabeled ligands. There was significant main effect ($F_{(2, 10)} = 6.32$, $P < 0.05$ by 1-way ANOVA). Post hoc analysis revealed that LTCx-to-CA1 ratio of ^{11}C-PiB was significantly higher than those of ^{125}I-DRM106 and ^{11}C-PBB3 (*$P < 0.05$, Bonferroni). Data are mean ± SD. Scale bars: A, 5 mm; B, C, 50 μm.

Tg2576 brain homogenates, suggesting that the terminal modification of Aβ may not change its binding sites for ^{125}I-DRM106. If so, binding sites for ^{125}I-DRM106 in AD patients and experimental animal models are more similar to each other, compared with that for ^{11}C-PiB. As evidence, the ratio of maximum binding values of ^{125}I-DRM106 for high-affinity binding sites in a 20-mo-old Tg2576 mouse to that in AD brain was proximately 0.17, much higher than that of ^{11}C-PiB (ratio of maximum binding values in a 15-mo-old APP/PS1 double-transgenic mouse to AD brain was below 0.001) (*20*). On the basis of the BP values for high- and low-affinity binding sites in Tg2576 mouse brain being approximately 27 and 14, respectively, the percentage of BP for high-affinity binding is approximately 65%. Likewise, the percentage of BP for high-affinity binding in AD brain is approximately 69% (Table 1). These 2 similar values may imply a similarity of composition of binding sites for ^{125}I-DRM106 in Tg2576 and AD brains, largely differing from that seen in ^{11}C-PiB binding to the AD model mouse and patient brains (percentage of BP for high-affinity binding was ~37% and 92% in the AD model mouse and patient brains, respectively) (*20*). This similarity in values suggests that $^{123/125}$I-DRM106 is more suitable than ^{11}C-PiB for translational research of the progression of amyloid pathology when using existing APP transgenic mouse models, most of which express numerous dense-cored, but not AD-like, diffuse plaques.

CONCLUSION

In this study, we have successfully captured Aβ deposition in a living AD model mouse with a newly developed SPECT agent, ^{123}I-DRM106. Given that its capacity was not inferior to ^{11}C-PiB for detecting Aβ deposition, ^{123}I-DRM106 has a high potential for further clinical application and, in fact, might preferentially capture the deposition of dense-cored/neuritic plaques.

DISCLOSURE

The costs of publication of this article were defrayed in part by the payment of page charges. Therefore, and solely to indicate this fact, this article is hereby marked "advertisement" in accordance with 18 USC section 1734. This work was supported in part by grants-in-aid for Japan Advanced Molecular Imaging Program and Core Research for Evolutional Science and Technology and Scientific Research on Innovative Areas ("Brain Environment") 23111009 from the Ministry of Education, Culture, Sports, Science and Technology, Japan. No other potential conflict of interest relevant to this article was reported.

ACKNOWLEDGMENTS

We thank John Q. Trojanowski and Virginia M.-Y. Lee (Center for Neurodegenerative Disease Research, University of Pennsylvania) for kindly providing human tissue.

REFERENCES

1. Braak H, Braak E. Neuropathological staging of Alzheimer-related changes. *Acta Neuropathol (Berl).* 1991;82:239–259.
2. Maeda J, Ji B, Irie T, et al. Longitudinal, quantitative assessment of amyloid, neuroinflammation, and anti-amyloid treatment in a living mouse model of Alzheimer's disease enabled by positron emission tomography. *J Neurosci.* 2007; 27:10957–10968.
3. Klunk WE, Engler H, Nordberg A, et al. Imaging brain amyloid in Alzheimer's disease with Pittsburgh Compound-B. *Ann Neurol.* 2004;55:306–319.
4. Engler H, Forsberg A, Almkvist O, et al. Two-year follow-up of amyloid deposition in patients with Alzheimer's disease. *Brain.* 2006;129:2856–2866.
5. Ikonomovic MD, Klunk WE, Abrahamson EE, et al. Post-mortem correlates of in vivo PiB-PET amyloid imaging in a typical case of Alzheimer's disease. *Brain.* 2008;131:1630–1645.
6. Leinonen V, Alafuzoff I, Aalto S, et al. Assessment of β-amyloid in a frontal cortical brain biopsy specimen and by positron emission tomography with carbon 11-labeled Pittsburgh Compound B. *Arch Neurol.* 2008;65:1304–1309.
7. Okello A, Koivunen J, Edison P, et al. Conversion of amyloid positive and negative MCI to AD over 3 years: an ^{11}C-PIB PET study. *Neurology.* 2009;73: 754–760.
8. Zhang W, Kung MP, Oya S, et al. ^{18}F-labeled styrylpyridines as PET agents for amyloid plaque imaging. *Nucl Med Biol.* 2007;34:89–97.

9. Choi SR, Golding G, Zhuang Z, et al. Preclinical properties of ^{18}F-AV-45: a PET agent for Aβ plaques in the brain. *J Nucl Med.* 2009;50:1887–1894.
10. Hampel H, Wilcock G, Andrieu S, et al. Biomarkers for Alzheimer's disease therapeutic trials. *Prog Neurobiol.* 2011;95:579–593.
11. Cselényi Z, Jonhagen ME, Forsberg A, et al. Clinical validation of ^{18}F-AZD4694, an amyloid-β-specific PET radioligand. *J Nucl Med.* 2012;53:415–424.
12. Kung MP, Hou C, Zhuang ZP, et al. Characterization of IMPY as a potential imaging agent for β-amyloid plaques in double transgenic PSAPP mice. *Eur J Nucl Med Mol Imaging.* 2004;31:1136–1145.
13. Kung MP, Hou C, Zhuang ZP, et al. IMPY: an improved thioflavin-T derivative for in vivo labeling of β-amyloid plaques. *Brain Res.* 2002;956:202–210.
14. Hsiao IT, Huang CC, Hsieh CJ, et al. Correlation of early-phase ^{18}F-florbetapir (AV-45/Amyvid) PET images to FDG images: preliminary studies. *Eur J Nucl Med Mol Imaging.* 2012;39:613–620.
15. Newberg AB, Wintering NA, Plossl K, et al. Safety, biodistribution, and dosimetry of ^{123}I-IMPY: a novel amyloid plaque-imaging agent for the diagnosis of Alzheimer's disease. *J Nucl Med.* 2006;47:748–754.
16. Song PJ, Bernard S, Sarradin P, et al. IMPY, a potential β-amyloid imaging probe for detection of prion deposits in scrapie-infected mice. *Nucl Med Biol.* 2008;35:197–201.
17. Kung MP, Weng CC, Lin KJ, et al. Amyloid plaque imaging from IMPY/SPECT to AV-45/PET. *Chang Gung Med J.* 2012;35:211–218.
18. Chen CJ, Bando K, Ashino H, et al. Synthesis and biological evaluation of novel radioiodinated imidazopyridine derivatives for amyloid-β imaging in Alzheimer's disease. *Bioorg Med Chem.* 2014;22:4189–4197.
19. Maruyama M, Shimada H, Suhara T, et al. Imaging of tau pathology in a tauopathy mouse model and in Alzheimer patients compared to normal controls. *Neuron.* 2013;79:1094–1108.
20. Klunk WE, Lopresti BJ, Ikonomovic MD, et al. Binding of the positron emission tomography tracer Pittsburgh compound-B reflects the amount of amyloid-β in Alzheimer's disease brain but not in transgenic mouse brain. *J Neurosci.* 2005;25:10598–10606.
21. Ono M, Cheng Y, Kimura H, et al. Development of novel ^{123}I-labeled pyridyl benzofuran derivatives for SPECT imaging of β-amyloid plaques in Alzheimer's disease. *PLoS ONE.* 2013;8:e74104.
22. Maya Y, Okumura Y, Onishi T, et al. Preclinical and clinical properties of [123I] ABC557: a novel radioiodinated SPECT agent for imaging b-amyloid in the brain. Poster presented at: Alzheimer Association International Conference; July 12–16, 2014; Copenhagen, Denmark.
23. Kawarabayashi T, Younkin LH, Saido TC, et al. Age-dependent changes in brain, CSF, and plasma amyloid β protein in the Tg2576 transgenic mouse model of Alzheimer's disease. *J Neurosci.* 2001;21:372–381.
24. Snellman A, Rokka J, Lopez-Picon FR, et al. Pharmacokinetics of [^{18}F]flutemetamol in wild-type rodents and its binding to β amyloid deposits in a mouse model of Alzheimer's disease. *Eur J Nucl Med Mol Imaging.* 2012;39: 1784–1795.
25. Ito H, Shinotoh H, Shimada H, et al. Imaging of amyloid deposition in human brain using positron emission tomography and [^{18}F]FACT: comparison with [^{11}C]PIB. *Eur J Nucl Med Mol Imaging.* 2014;41:745–754.

JNM The Journal of NUCLEAR MEDICINE

In Vivo SPECT Imaging of Amyloid-β Deposition with Radioiodinated Imidazo[1,2-*a*]Pyridine Derivative DRM106 in a Mouse Model of Alzheimer's Disease

Chun-Jen Chen, Kazunori Bando, Hiroki Ashino, Kazumi Taguchi, Hideaki Shiraishi, Keiji Shima, Osuke Fujimoto, Chiemi Kitamura, Satoshi Matsushima, Keisuke Uchida, Yuto Nakahara, Hiroyuki Kasahara, Takao Minamizawa, Cheng Jiang, Ming-Rong Zhang, Maiko Ono, Masaki Tokunaga, Tetsuya Suhara, Makoto Higuchi, Kazutaka Yamada and Bin Ji

J Nucl Med. 2015;56:120-126.
Published online: December 4, 2014.
Doi: 10.2967/jnumed.114.146944

The Journal of Nuclear Medicine is published monthly.
SNMMI | Society of Nuclear Medicine and Molecular Imaging
1850 Samuel Morse Drive, Reston, VA 20190.
(Print ISSN: 0161-5505, Online ISSN: 2159-662X)

SNMMI SOCIETY OF NUCLEAR MEDICINE AND MOLECULAR IMAGING

JNM The Journal of NUCLEAR MEDICINE

Radiosynthesis, Photoisomerization, Biodistribution, and Metabolite Analysis of ^{11}C-PBB3 as a Clinically Useful PET Probe for Imaging of Tau Pathology

Hiroki Hashimoto, Kazunori Kawamura, Nobuyuki Igarashi, Makoto Takei, Tomoya Fujishiro, Yoshiharu Aihara, Satoshi Shiomi, Masatoshi Muto, Takehito Ito, Kenji Furutsuka, Tomoteru Yamasaki, Joji Yui, Lin Xie, Maiko Ono, Akiko Hatori, Kazuyoshi Nemoto, Tetsuya Suhara, Makoto Higuchi and Ming-Rong Zhang

J Nucl Med. 2014;55:1532-1538.
Published online: June 24, 2014.
Doi: 10.2967/jnumed.114.139550

The Journal of Nuclear Medicine is published monthly.
SNMMI | Society of Nuclear Medicine and Molecular Imaging
1850 Samuel Morse Drive, Reston, VA 20190.
(Print ISSN: 0161-5505, Online ISSN: 2159-662X)

SNMMI SOCIETY OF NUCLEAR MEDICINE AND MOLECULAR IMAGING

Radiosynthesis, Photoisomerization, Biodistribution, and Metabolite Analysis of ^{11}C-PBB3 as a Clinically Useful PET Probe for Imaging of Tau Pathology

Hiroki Hashimoto[1], Kazunori Kawamura[1], Nobuyuki Igarashi[1,2], Makoto Takei[1,2], Tomoya Fujishiro[1,2], Yoshiharu Aihara[1,2], Satoshi Shiomi[1,2], Masatoshi Muto[1,2], Takehito Ito[1,3], Kenji Furutsuka[1,3], Tomoteru Yamasaki[1], Joji Yui[1], Lin Xie[1], Maiko Ono[1], Akiko Hatori[1], Kazuyoshi Nemoto[1], Tetsuya Suhara[1], Makoto Higuchi[1], and Ming-Rong Zhang[1]

[1]Molecular Imaging Center, National Institute of Radiological Sciences, Chiba, Japan; [2]Tokyo Nuclear Services Co., Ltd., Tokyo, Japan; and [3]SHI Accelerator Service Ltd., Tokyo, Japan

2-((1*E*,3*E*)-4-(6-(¹¹C-methylamino)pyridin-3-yl)buta-1,3-dienyl) benzo[*d*]thiazol-6-ol (¹¹C-PBB3) is a clinically useful PET probe that we developed for in vivo imaging of tau pathology in the human brain. To ensure the availability of this probe among multiple PET facilities, in the present study we established protocols for the radiosynthesis and quality control of ¹¹C-PBB3 and for the characterization of its photoisomerization, biodistribution, and metabolism. **Methods:** ¹¹C-PBB3 was synthesized by reaction of the *tert*-butyldimethylsilyl desmethyl precursor (**1**) with ¹¹C-methyl iodide using potassium hydroxide as a base, followed by deprotection. Photoisomerization of ¹¹C-PBB3 under fluorescent light was determined. The biodistribution and metabolite analysis of ¹¹C-PBB3 was determined in mice using the dissection method. **Results:** ¹¹C-PBB3 was synthesized with 15.4% ± 2.8% radiochemical yield (decay-corrected, n = 50) based on the cyclotron-produced ¹¹C-CO_2 and showed an averaged synthesis time of 35 min from the end of bombardment. The radiochemical purity and specific activity of ¹¹C-PBB3 were 98.0% ± 2.3% and 180.2 ± 44.3 GBq/μmol, respectively, at the end of synthesis (n = 50). ¹¹C-PBB3 showed rapid photoisomerization, and its radiochemical purity decreased to approximately 50% at 10 min after exposure to fluorescent light. After the fluorescent light was switched off, ¹¹C-PBB3 retained more than 95% radiochemical purity over 60 min. A suitable brain uptake (1.92% injected dose/g tissue) of radioactivity was observed at 1 min after the probe injection, which was followed by rapid washout from the brain tissue. More than 70% of total radioactivity in the mouse brain homogenate at 5 min after injection represented the unchanged ¹¹C-PBB3, despite its rapid metabolism in the plasma. **Conclusion:** ¹¹C-PBB3 was produced with sufficient radioactivity and high quality, demonstrating its clinical utility. The present results of radiosynthesis, photoisomerization, biodistribution, and metabolite analysis could be helpful for the reliable production and application of ¹¹C-PBB3 in diverse PET facilities.

Key Words: tau pathology; Alzheimer disease; PET; ¹¹C-PBB3; photoisomerization

J Nucl Med 2014; 55:1532–1538
DOI: 10.2967/jnumed.114.139550

Received Feb. 24, 2014; revision accepted May 19, 2014.
For correspondence or reprints contact: Ming-Rong Zhang, Molecular Probe Program, Molecular Imaging Center, National Institute of Radiological Sciences, 4-9-1 Anagawa, Inage-Ku, Chiba 263-8555, Japan.
E-mail: zhang@nirs.go.jp
Published online Jun. 24, 2014.

Accumulation of intracellular tau fibrils is a neuropathologic hallmark of Alzheimer disease (AD) and related tau-positive neurodegenerative disorders, which are collectively referred to as tauopathies (*1*). Understanding of the mechanistic roles played by pathologic tau in AD and related tauopathies has stimulated increasing interest in the development of imaging probes that facilitate visualization of tau pathology in the brains of living humans and animal models of tauopathies (*1*). ¹⁸F-FDDNP (Fig. 1) was applied to PET imaging of intraneuronal neurofibrillary tangles for the first time (*2*). However, ¹⁸F-FDDNP showed a relatively low contrast and selectivity for tau lesions versus β amyloid in in vitro autoradiograms and PET images of AD brains (*3*). In addition to ¹⁸F-FDDNP, researchers have developed several promising PET probes for imaging tau protein in the brain (*4–10*). Among these radioprobes, ¹⁸F-T807, ¹⁸F-T808, ¹⁸F-THK523, and ¹⁸F-THK5105 (Fig. 1) have been used in clinical studies for AD patients (*6,8–10*), whereas its capability of capturing tau aggregates in non-AD tauopathies and transgenic animal models is yet to be determined.

Recently, we developed a new class of tau ligands, phenyl/pyridinyl butadienyl benzothiazoles/benzothiazoliums (PBBs). In vivo optical imaging of a transgenic mouse model demonstrated rapid and sensitive detection of intraneuronal tau inclusions by intravenous administration of these ligands, which are intrinsically fluorescent (*11*). Selected from these ligands, three ¹¹C-labeled compounds were synthesized and evaluated for their potential as PET probes for imaging tau pathology in tau transgenic mouse models (*11*). After preclinical evaluation, 2-((1*E*,3*E*)-4-(6-(¹¹C-methylamino)pyridin-3-yl)buta-1,3-dienyl)benzo[*d*]thiazol-6-ol (¹¹C-PBB3, Fig. 1) was applied to clinical PET studies and was demonstrated to effectively display tau pathology in patients with AD and non-AD tauopathies. Notably, the high-level retention of ¹¹C-PBB3 in the AD hippocampus wherein tau pathology is enriched sharply contrasted with that of a β-amyloid PET probe, ¹¹C-Pittsburgh compound B (¹¹C-PIB) (*11,12*).

Our previous study was focused on the development of PBBs and the application of ¹¹C-PBB3 to PET imaging of a mouse model and human brains (*11*). Meanwhile, the growing interest in the clinical use of ¹¹C-PBB3 in many PET facilities motivated us to establish protocols for its radiosynthesis and quality control and to characterize its chemical stability and its pharmacokinetic

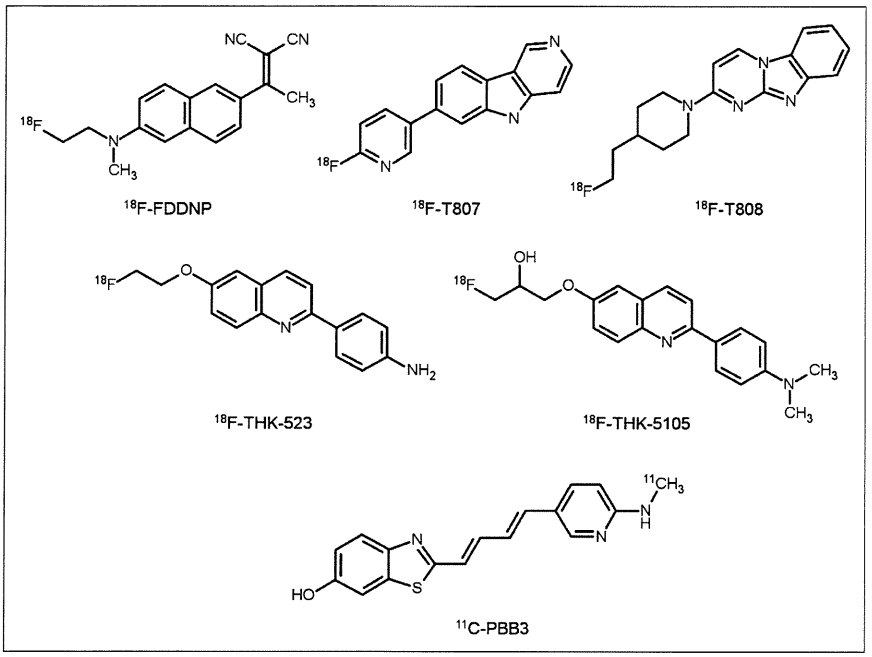

FIGURE 1. Chemical structures of PET probes for imaging of tau pathology in clinical use.

and metabolic properties. Here, we determined the radiosynthetic conditions for ^{11}C-PBB3 to obtain an appropriate amount of radioactivity with reliable quality for clinical application. Because of the chemical structure of pyridylbutadienylbenzothiazole in ^{11}C-PBB3, which is considered to easily undergo photoisomerization by exposure to ultraviolet light (*13*), we monitored the progress of photoisomerization of ^{11}C-PBB3 under fluorescent light and investigated how to prevent it during radiosynthesis and quality control. To validate whether the radioactive signals in the mouse and human brains were derived from ^{11}C-PBB3 itself, we performed metabolite analysis of ^{11}C-PBB3 for the mouse plasma and brain homogenate.

MATERIALS AND METHODS

General

PBB3 and its precursor (5-((1*E*,3*E*)-4-(6-(*tert*-butyldimethylsilyloxy)-benzo[*d*]thiazol-2-yl)buta-1,3-dienyl)pyridin-2-amine (**1**, Fig. 2) for radiosynthesis were synthesized and supplied from the NARD Institute. Commercially available reagents and organic solvents (Sigma-Aldrich and Wako Pure Chemical Industries) were used without further purification. ^{11}C was produced by ^{14}N (p, α)^{11}C nuclear reaction using a CYPRIS HM18 cyclotron (Sumitomo Heavy Industries). Effluent radioactivity was monitored using a NaI (Tl) scintillation detector system (Gabi Star PET; Raytest). If not otherwise stated, radioactivity was determined using an IGC-3R Curiemeter (Aloka).

Male ddY mice were purchased from Japan SLC Inc. Animals were maintained and handled in accordance with the recommendations of the U.S. National Institutes of Health and the guidelines of the National Institute of Radiologic Sciences. Animal experiments were approved by the Animal Ethics Committee of the National Institute of Radiologic Sciences. Male ddY mice (35.2 ± 2.2 g) were fed ad libitum.

Radiosynthesis of ^{11}C-PBB3

^{11}C-methyl iodide (^{11}C-CH_3I) was synthesized from cyclotron-produced ^{11}C-CO_2 using an automated synthesis system developed in-house (*14*). The produced ^{11}C-CH_3I was trapped in a mixture of the *tert*-butyldimethylsilyl group-protected desmethyl precursor **1** (0.9–1.1 mg) in anhydrous dimethylsulfoxide (0.15 mL) and KOH (10 mg) suspended in anhydrous dimethylsulfoxide (0.3 mL) at room temperature. Heating the reaction mixture at 125°C for 5 min produced 5-((1*E*,3*E*)-4-(6-(*tert*-butyldimethylsilyloxy)benzo[*d*]thiazol-2-yl)buta-1,3-dienyl)-*N*-2-^{11}C-methylpyridin-2-amine (^{11}C-**2**). Subsequent deprotection of the *tert*-butyldimethylsilyl group in ^{11}C-**2** was performed using H_2O (0.2 mL) at 50°C for 2 min. After 1.5 mL of the high-performance liquid chromatography (HPLC) solvent was added to the reaction vessel, the radioactive mixture was loaded into a preparative HPLC system (Jasco) for separation. The HPLC conditions were as follows: Atlantis T3 (5 μm, 10-mm internal diameter [i.d.] × 150 mm; Waters); acetonitrile/50 mM sodium phosphate buffer (pH 7.0) (20/30, v/v); 6.0 mL/min; 379-nm ultraviolet light. The fraction corresponding to ^{11}C-PBB3 (retention time [t_R], ~7 min) was collected into a flask in which 25% ascorbic acid (0.4 mL) and polysorbate-80 (0.075 mL) in ethanol (0.3 mL) had been added before radiosynthesis, and was then evaporated to dryness. The residue was dissolved in physiologic saline (6–12 mL) and sterilized with a Millex-GS filter (Millipore). An amber vial was filled with the formulated product.

All radiosynthesis and subsequent quality control procedures were performed without fluorescent light to prevent photoisomerization of ^{11}C-PBB3. If necessary, an ultraviolet-cutoff flashlight (green light, LED-41VIS525; OptoCode) was used to monitor these procedures for a short time.

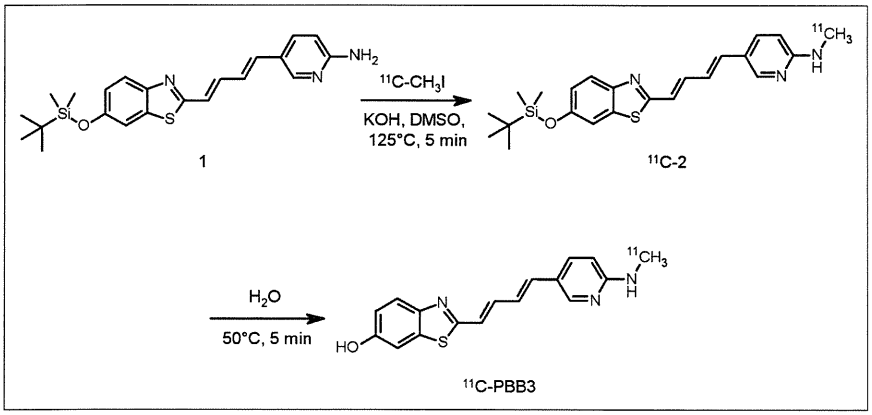

FIGURE 2. Radiosynthesis of ^{11}C-PBB3.

Determination of Radiochemical Purity and Photoisomerization

With the fluorescent light switched off, the final product solution of ^{11}C-PBB3 was analyzed using an HPLC system (515 pump and 2487 ultraviolet detector; Waters) and an XBridge Shield RP18 column (2.5 μm, 3.0 mm i.d. × 50 mm; Waters). A mixture of 90%

aqueous acetonitrile and 50 mM ammonium phosphate buffer (pH 9.3) (50/50 [0–1.2 min] and then 70/30 [1.2 min and onward], v/v) was used as the mobile phase. The t_R of ^{11}C-PBB3 was approximately 1.1 min at 1.0 mL/min. The identity was confirmed by coinjection with an authentic PBB3 sample. The specific activity was calculated by comparison of the assayed radioactivity to the carrier mass, which was measured on the basis of its ultraviolet peak at 379 nm. To determine the radiochemical stability of ^{11}C-PBB3, the formulated product was maintained for 60 min at room temperature without fluorescent light. An analytic sample was taken from the formulated solution to measure the radiochemical purity again.

For comparison, a portion of the ^{11}C-PBB3 injection sample was transferred to a colorless vial and maintained for 60 min at room temperature under fluorescent light. Analytic samples were taken from this vial to measure the radiochemical purity at 1, 10, and 60 min.

Quality Control

In addition to determination of radiochemical purity and specific activity, the physical appearance of the ^{11}C-PBB3 injection was checked by visual inspection (*15*). pH was measured using a pH meter (F-71; Horiba) and a probe (9618-10D; Horiba). Sterility was tested using a soybean-casein digest broth (Merck) incubated with the injection sample at 20°C–25°C for 14 d and fluid thioglycollate medium (Merck) incubated with the sample at 30°C–35°C for 14 d. Absence of culture growth after 14 d indicates sterility (*16*). The endotoxin content in the injection sample was measured using a toxinometer (ET-6000; Wako) (*17*). Residual organic solvents (acetonitrile and ethanol) were measured using a gas chromatography system (7890; Agilent Technologies) (*18*). A DB-WAX column (0.50 μm, 0.53-mm i.d. × 30 m; Agilent Technologies) was maintained at 40°C (0–8 min), raised to 120°C (8–28 min), and kept at 120°C (28–33 min). The makeup gas was nitrogen (99.9995%, 50 mL/min), and the carrier gas was helium (99.995%, 4 mL/min). A flame ionization detector was used.

Biodistribution Study

^{11}C-PBB3 (1.6 MBq in 0.1 mL, 49.6 GBq/μmol) was injected into the tail vein of mice (n = 4 for each time point) without fluorescent light. The blood, heart, lung, spleen, liver, small intestine, testis, kidney, muscle, and brain were dissected at 1, 5, 15, 30, and 60 min after injection. The radioactivity in each tissue was measured using a γ counter (1480 Wizard 3; Perkin-Elmer) and expressed as follows: uptake [percentage injected dose (%ID)/g] = [tissue radioactivity (cps) × 100/tissue weight (g)]/injected dose (cps). All measured radioactivity values were corrected for decay.

Metabolite Analysis in Brain and Plasma

^{11}C-PBB3 (33.3–37 MBq in 0.1–0.2 mL, 51.9 ± 18.2 GBq/μmol) was injected into the tail vein of mice (n = 3 for each time point), and the mice were sacrificed by cervical dislocation at 1 and 5 min after injection. Blood samples were obtained and centrifuged at 15,000 rpm for 1 min at 4°C. The plasma (0.5 mL) was separated and transferred to a tube containing acetonitrile (0.5 mL). The mixture was stirred in a vortex mixer and centrifuged at 15,000 rpm for 2 min to separate the precipitate from the aqueous phase.

The half brain was placed in test tubes, each containing 2.5 mL of ice-cooled saline, and homogenized (SilentCrusher-S; Heidolph Instruments). Radioactivity (%ID/g) in the left brain was measured at the same time. The homogenized brain tissue (0.5 mL) was transferred to a tube containing acetonitrile (0.5 mL) and centrifuged (15,000 rpm, 2 min, 4°C). The precipitate and supernatant were separated and measured for radioactivity. The supernatants of the plasma and brain homogenates were analyzed using an HPLC system equipped with a highly sensitive detector for radioactivity (*19*). The HPLC system and conditions were as follows: pump, PU-2089 plus (Jasco); ultraviolet detector, UV-2075 (Jasco); NaI(Tl) scintillation detector (S-2493A; OKEN); precolumn, XBridge Prep C18 Guard Cartridge (5 μm, 10 mm i.d. × 10 mm; Waters); main column, XBridge OST C18 (2.5 μm, 10 mm i.d. × 50 mm; Waters); mobile phase, 90% aqueous acetonitrile/0.02 M sodium phosphate buffer (pH 7.0) (30/70 [0–4 min], 40/60 to 70/30 [4–7 min], v/v); flow rate, 8.0 mL/min; t_R, ^{11}C-PBB3, 5 min. All the procedures in this section were conducted with the fluorescent light switched off.

RESULTS

Radiosynthesis of ^{11}C-PBB3

^{11}C-PBB3 was synthesized by *N*-methylation of the desmethyl precursor **1** with ^{11}C-CH_3I using KOH as a base (Fig. 2), followed by deprotection of the *tert*-butyldimethylsilyl group in the intermediate ^{11}C-**2** with water. After the reaction, HPLC separation (Fig. 3), and formulation, ^{11}C-PBB3 was successfully obtained with a sufficient amount of radioactivity. At the end of synthesis, ^{11}C-PBB3 of 1.6–3.1 GBq was obtained as an injectable solution of sterile normal saline after 30–35 min of proton bombardment at a beam current of 18 μA. The decay-corrected radiochemical yield of ^{11}C-PBB3 based on ^{11}C-CO_2 was 15.4% ± 2.8% (n = 50) at the end of bombardment, and the specific activity was 180.2 ± 44.3 GBq/μmol (n = 50) at the end of synthesis. The averaged radiochemical purity of the ^{11}C-PBB3 product in an amber vial was 98.0% ± 2.3% (Fig. 4A) and remained greater than 95% after 60 min (Fig. 4B) without fluorescent light. The total synthesis time was approximately 35 min from the end of bombardment.

Photoisomerization

Figures 4C–4E show the photoisomerization of ^{11}C-PBB3 in a colorless vial under fluorescent light. At 1 min after exposure to the fluorescent light, the radiochemical purity of ^{11}C-PBB3 decreased to 77%. From 10 to 60 min, its radiochemical purity remained approximately 50%. The chemical structure of the ^{11}C-impurity was not identified but was assumed to be the *Z, Z* or *E, Z* isomer of ^{11}C-PBB3.

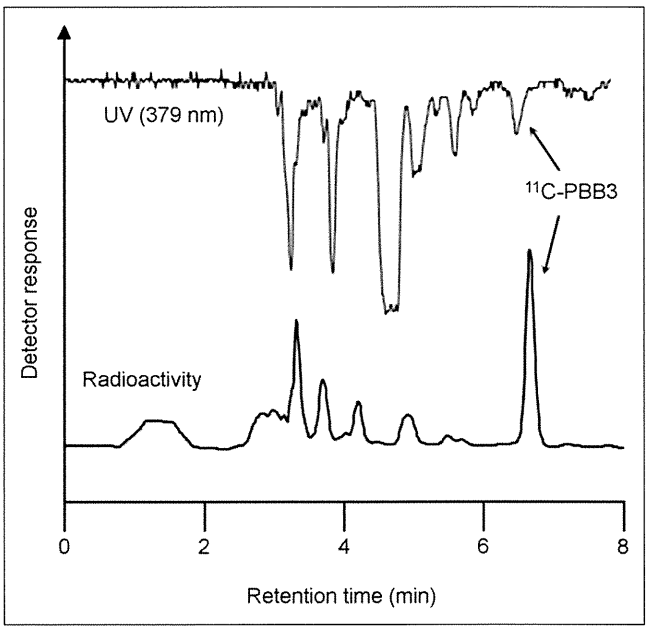

FIGURE 3. Typical preparative HPLC chromatogram of ^{11}C-PBB3.

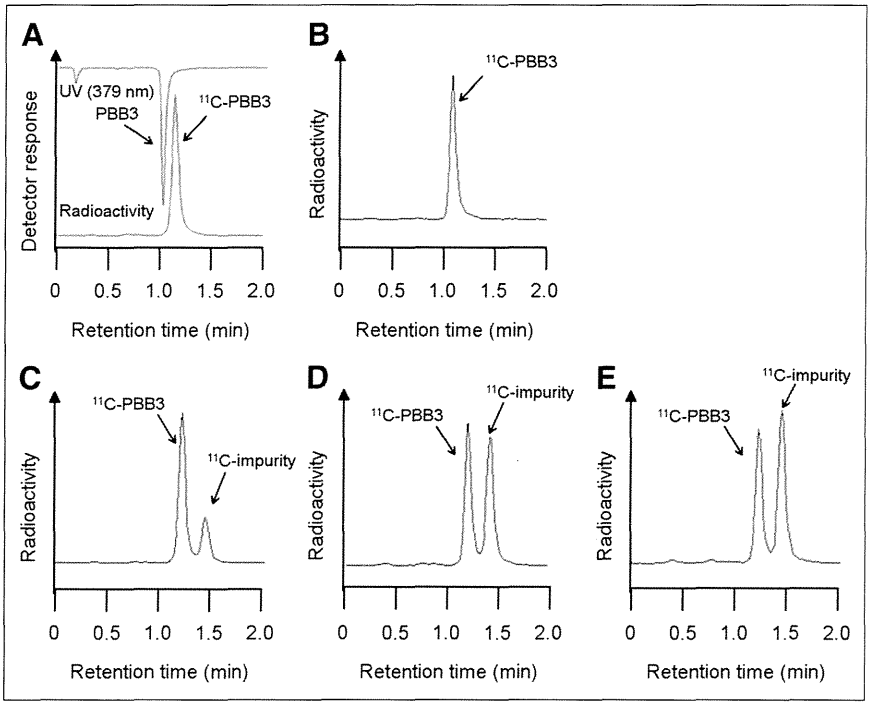

FIGURE 4. Typical analytic HPLC chromatograms of ^{11}C-PBB3. Analyses were performed without (A and B) and with (C–E) fluorescent light. Identity of ^{11}C-PBB3 was confirmed by co-injection with authentic PBB3 sample immediately after formulation (A) and at 60 min (B), 1 min (C), 10 min (D), and 60 min (E).

Quality Control

Table 1 summarizes the results of the quality control assessment for 3 different lots of ^{11}C-PBB3 production. The physical appearance of the product was clear and without particles. The pH was 6.7 ± 0.8. In sterility testing, no viable bacteria or microorganisms were observed in soybean-casein digest broth or fluid thioglycollate medium. The endotoxin content was undetectable (<0.7 endotoxin units/maximum volume). The radiochemical purity of ^{11}C-PBB3 was 98.2% ± 2.2% (n = 3) at the end of synthesis and was within the range of 97.0% ± 0.8% after 60 min. The residual amounts of ethanol and acetonitrile in the ^{11}C-PBB3 injection sample were to be 6.7 ± 0.6 ppm and 1 ppm, respectively.

Biodistribution Study

Table 2 shows the tissue distribution of radioactivity in the whole body of mice at 1, 5, 15, 30, and 60 min after injection of ^{11}C-PBB3. Uptake in most tissues was the highest at 1 min among all sampling time points. The radioactivity levels in the blood, heart, lung, testis, muscle, and brain decreased rapidly after initial uptake, whereas the radioactivity in the liver, spleen, small intestine, and kidney reduced gradually after 5 min. The radioactivity in all tissues except the small intestine cleared to less than 1 %ID/g at 60 min. Brain uptake was 1.92 %ID/g at 1 min and then decreased rapidly to 0.03 %ID/g at 60 min.

Metabolite Analysis in Brain and Plasma

Figure 5 shows the HPLC chromatograms for the plasma and brain homogenate samples after injection of ^{11}C-PBB3. In the plasma, the percentage of ^{11}C-PBB3 rapidly decreased and a radiolabeled metabolite was observed as early as 1 min after injection (Fig. 5A). The fraction corresponding to unchanged ^{11}C-PBB3 in the plasma was 1.9% ± 0.53% at 5 min (Fig. 5B) and was not detectable at 15 min (data not shown). The radiolabeled metabolite was more polar than ^{11}C-PBB3, as estimated by its t_R (2.0 min) on the HPLC charts. Despite the rapid metabolism in plasma, the percentage of unchanged ^{11}C-PBB3 in the brain homogenate was 82% at 1 min (Fig. 5C) and 70% at 5 min (Fig. 5D). A radiolabeled metabolite was also detected in the HPLC charts of the brain samples, and its t_R was similar to that of the metabolite in the plasma. Calculated from the total brain uptake (%ID/g), which was simultaneously measured for the same mice, radioactivity levels representing unchanged ^{11}C-PBB3 and ^{11}C-metabolite in the brain were found to be 1.58 ± 0.25 and 0.35 ± 0.06 %ID/g, respectively, at 1 min and 0.83 ± 0.06 and 0.35 ± 0.04 %ID/g, respectively, at 5 min. Recovery of radioactivity from HPLC analysis for all samples was greater than 95%. Because of the low

TABLE 1
Quality Control for ^{11}C-PBB3 Productions (n = 3)

Test	Acceptance criterion	Lot 1	Lot 2	Lot 3
Radioactivity (GBq)	Not less than 0.185	1.56	1.88	1.82
Specific activity (GBq/μmol)	Not less than 3.7	141.2	186.6	138.2
Bacterial endotoxin (international units/maximum dose)	<175	<0.5	<0.5	<0.5
Sterility	No bacterial growth	No bacterial growth	No bacterial growth	No bacterial growth
pH	4.5–8.0	6.8	6.6	6.8
Radiochemical purity after 60 min	Not less than 95% of total radioactivity	96.1%	97.5%	97.5%
Residual solvent (ppm)				
Ethanol	<5,000	7	6	7
Acetonitrile	<410	1	1	1

TABLE 2
Biodistribution for ^{11}C-PBB3 in Mice

Site	1 min	5 min	15 min	30 min	60 min
Blood	4.34 ± 0.38	3.06 ± 0.65	1.27 ± 0.19	0.64 ± 0.12	0.12 ± 0.03
Heart	5.98 ± 0.72	2.10 ± 0.17	0.72 ± 0.07	0.32 ± 0.03	0.06 ± 0.02
Lung	12.51 ± 1.06	3.58 ± 2.46	2.12 ± 0.20	1.07 ± 0.28	0.21 ± 0.07
Spleen	1.62 ± 0.40	3.49 ± 2.48	0.43 ± 0.03	0.23 ± 0.07	0.07 ± 0.01
Liver	8.01 ± 1.01	14.81 ± 1.29	9.01 ± 1.04	4.42 ± 0.76	0.88 ± 0.17
Small intestine	14.71 ± 3.97	45.58 ± 7.82	29.64 ± 8.02	16.72 ± 5.34	3.57 ± 1.44
Testis	0.56 ± 0.09	1.15 ± 0.54	0.68 ± 0.22	0.47 ± 0.10	0.09 ± 0.01
Kidney	12.49 ± 1.19	10.55 ± 0.81	4.36 ± 0.40	1.80 ± 0.26	0.30 ± 0.05
Muscle	2.59 ± 0.25	1.33 ± 0.23	0.55 ± 0 .07	0.22 ± 0.02	0.04 ± 0.04
Brain	1.92 ± 0.13	0.97 ± 0.06	0.27 ± 0.02	0.11 ± 0.04	0.03 ± 0.01

Data are mean (± SD) %ID/g tissue (n = 4).

radioactivity level, no further metabolite analysis was performed for the brain samples collected beyond 5 min.

DISCUSSION

In this study, ^{11}C-PBB3, a PET probe clinically used for imaging tau pathology in the human brain, was reliably synthesized with sufficient radioactivity and high quality. The metabolite analysis demonstrated the presence of unchanged ^{11}C-PBB3 as the major radiolabeled component in the mouse brain despite its rapid metabolism in the plasma.

For the radiosynthesis of ^{11}C-PBB3, the *tert*-butyldimethylsilyl group-protected desmethyl compound **1** was designed as the precursor. ^{11}C-methylation of **1** and subsequent deprotection of ^{11}C-**2** gave ^{11}C-PBB3 in a 2-step, 1-pot process (Fig. 2). We initially attempted to perform ^{11}C-methylation of **1** using ^{11}C-CH_3OTf and no base, as is done for the synthesis of ^{11}C-Pittsburgh compound B, which was easily labeled by direct ^{11}C-methylation without requiring a base (*20*). However, this approach could not produce ^{11}C-**2,** indicating that the α-amino group in the pyridine ring of **1** did not have enough nucleophilicity to undergo ^{11}C-methylation without a base. Use of organic bases gave only trace amounts of ^{11}C-**2.** Because the low labeling efficiency with ^{11}C-CH_3OTf without a base could not be improved even by heating the reaction mixture to 150°C for 5 min, this approach was not pursued further.

We then used KOH powder as a base to form the salt of the amine group in situ for the ^{11}C-methylation of **1** with ^{11}C-CH_3I. The reaction conditions, including the amount of KOH, reaction solvent, time, and temperature, were optimized. It was found that the use of 10 mg of KOH, which was suspended in anhydrous dimethylsulfoxide for 20–30 s with an ultrasonic cleaner just before the synthesis, for reaction of 1 mg of **1** with ^{11}C-CH_3I at 125°C for 5 min could give the highest yield of ^{11}C-**2.**

To remove the protective *tert*-butyldimethylsilyl group in ^{11}C-**2,** we initially used tetrabutylammonium fluoride. Although the deprotection was successful, perfect removal of tetrabutylammonium fluoride and its decomposing residues in the final formulated product remained challenging. In place of tetrabutylammonium fluoride, we then used water to remove the *tert*-butyldimethylsilyl group. As expected, deprotection

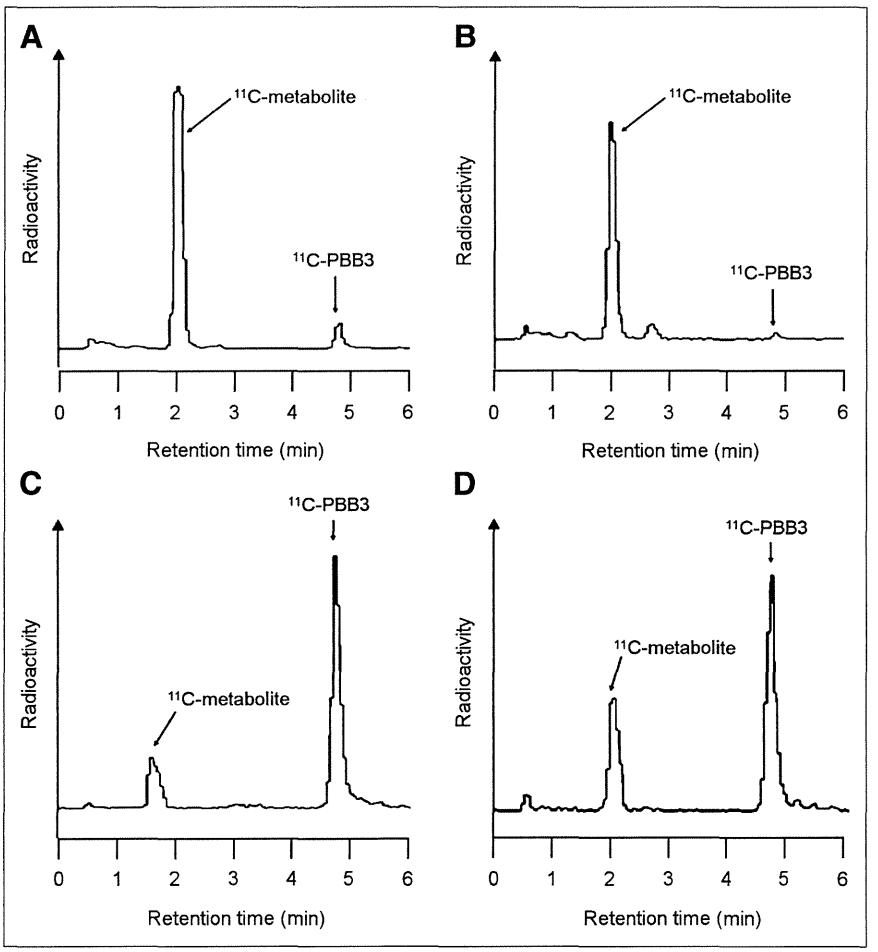

FIGURE 5. HPLC chromatograms for metabolite analysis of ^{11}C-PBB3 at 1 min in mouse plasma (A), at 5 min in mouse plasma (B), at 1 min in mouse brain (C), and at 5 min in mouse brain (D).

with alkali water at 50°C for 2 min proceeded perfectly. Indeed, alkali water was also used to remove the *tert*-butyldimethylsilyl group in the synthesis of ^{11}C-AZD2184, an imaging agent for β amyloid with structural similarity to ^{11}C-PBB3 (*21*).

Photoisomerization is a molecular behavior in which a structural change between isomers occurs because of photoexcitation. *E* and *Z* conversion is a representative behavior. Chemicals exhibiting this conversion include stilbene and azobenzene, in which the rotation or inversion around the double bond affords the isomerization between the 2 states (*13*). ^{11}C-PBB3 underwent rapid photoisomerization as a pyridylbutadienylbenzothiazole compound by exposure to fluorescent light as shown in the analytic HPLC charts (Figs. 4C–4E). Compared with ^{11}C-PBB3, its ^{11}C-isomer showed much less specific binding to tau in the brain sections of AD patients (Supplemental Fig. 1; supplemental materials are available at http://jnm.snmjournals.org). This photoisomerization could be prevented by switching off the fluorescent light. By cutting off all fluorescent light in the synthetic hot cell to perform the radiosynthesis, in particular HPLC separation and formulation, and using an amber vial to store the formulated product, ^{11}C-PBB3 was reliably obtained with high radiochemical purity without isomerization and radiolysis. All the results of quality control for the ^{11}C-PBB3 injection complied with our in-house quality control and quality assurance specifications (Table 1). These data have guaranteed a reliable supply of ^{11}C-PBB3 with sufficient radioactivity and high quality for clinical application.

The results of the biodistribution study of ^{11}C-PBB3 in mice suggest that the radioactivity might be cleared mainly via the hepatobiliary and intestinal reuptake pathways, with rapid washout from the body (Table 2). The present brain uptake indicates that ^{11}C-PBB3 easily passed through the blood–brain barrier, which is related to its lipophilicity (calculated logD, 3.30) (*11*). The effective dose estimate for ^{11}C-PBB3 was 3.28 μSv/MBq (Supplemental Table 1), which was comparable to that reported for other ^{11}C-labeled probes, including ^{11}C-Pittsburgh compound B (4.7 μSv/MBq) (*22*).

Metabolite analysis demonstrated that this probe was rapidly decomposed to a polar radiolabeled metabolite in the plasma (Fig. 5). Despite the high abundance in the plasma, this metabolite, which was more hydrophilic than ^{11}C-PBB3, showed limited entry into the brain. This finding indicates that uptake of radioactivity into the mouse brain was attributable mainly to unchanged ^{11}C-PBB3. The present data, taken together with the results of the previous metabolite analysis for human plasma (*11*), demonstrated that ^{11}C-PBB3 is rapidly metabolized to the same radiolabeled metabolite in mouse and human plasma, as evidenced by the similar t_Rs in the HPLC charts for plasma samples from these 2 species. The percentage of unchanged ^{11}C-PBB3 in human plasma at 3 min after injection was 7.8% ± 2.2%, and the metabolizing rate in human plasma was slightly slower than that in mouse plasma. These results indicate that the radioactive signals acquired by PET in the human brain may primarily reflect the kinetics of ^{11}C-PBB3. However, the influence of the low-grade uptake of radioactive metabolites into the brain on pharmacokinetic measures of ^{11}C-PBB3 should be clarified.

In both humans and mice, the rapid entry of ^{11}C-PBB3 into the brain and prompt reduction of the parent probe in the plasma imply that the levels of ^{11}C-PBB3 in the brain may be dependent largely on its first-pass extraction (*11*). This characteristic, along with its minimal nonspecific binding of ^{11}C-PBB3 to the myelin-rich components (*11*), resulted in a rapid washout of this probe from the brain, thereby reducing the background signal in the brain. Moreover, the significant contribution of the first-pass extraction to the radioprobe kinetics in the brain indicates that regional cerebral blood flow may be a critical determinant of the amount of ^{11}C-PBB3 entering the brain; accordingly, the specific binding of ^{11}C-PBB3 to tau lesions may be underestimated in areas with profound hypoperfusion. In fact, PET imaging with ^{11}C-PBB3 in the AD brain displayed high-contrast signals in the hippocampus and low nonspecific retention in the white matter and other myelin-rich regions (*11*). Although the brain uptake of ^{11}C-PBB3 is lower than that of ^{18}F-T807 and ^{11}C-Pittsburgh compound B (*5,11,23*), a relatively low concentration of free ^{11}C-PBB3 in the brain may be advantageous to its selective binding to high-affinity, low-capacity sites on tau fibrils, compared with the low-affinity, high-capacity binding sites on β amyloid (*11*).

A shortcoming of ^{11}C-PBB3 may be the presence of the radiolabeled metabolite in the mouse brain, although brain uptake of this metabolite was lower than that of unchanged ^{11}C-PBB3 in the brain. Determination of the metabolic pathway for ^{11}C-PBB3 is currently ongoing and should provide clues for the design of new probes with improved biostability. Identification of the chemical structure of the major ^{11}C-PBB3 metabolite should also be performed, and subsequent radiolabeling of this metabolite would facilitate evaluation of its plasma and brain kinetics and affinity for tau fibrils.

CONCLUSION

^{11}C-PBB3, a clinically useful PET probe for tau pathology in the brains of humans and transgenic mouse models, was successfully synthesized by reaction of *tert*-butyldimethylsilyl desmethyl precursor **1** with ^{11}C-CH_3I in the presence of KOH, followed by deprotection with water. We have so far achieved more than 200 productions of ^{11}C-PBB3 in our facility for various research purposes, including translational PET imaging of mouse models and clinical PET assessments of patients diagnosed as having AD and non-AD neurodegenerative disorders. The present results demonstrate the reliable production and widespread clinical potential of ^{11}C-PBB3.

DISCLOSURE

The costs of publication of this article were defrayed in part by the payment of page charges. Therefore, and solely to indicate this fact, this article is hereby marked "advertisement" in accordance with 18 USC section 1734. This study was funded in part by Grants-in-Aid for the Japan Advanced Molecular Imaging Program, Scientific Research (B) (23390235), Core Research for Evolutional Science and Technology, and Scientific Research on Innovative Areas (Brain Environment) (23111009) from the Ministry of Education, Culture, Sports, Science, and Technology, Japan. Drs. Suhara, Higuchi, and Zhang are named as inventors on patent application 0749006WO1, claiming subject matter related to the results described in this paper. No other potential conflict of interest relevant to this article was reported.

REFERENCES

1. Ballatore C, Lee VMY, Trojanowski JQ. Tau-mediated neurodegeneration in Alzheimer's disease and related disorders. *Nat Rev Neurosci.* 2007;8:663–672.
2. Small GW, Kepe V, Ercoli LM, et al. PET of brain amyloid and tau in mild cognitive impairment. *N Engl J Med.* 2006;355:2652–2663.
3. Thompson PW, Ye L, Morgenstern JL, et al. Interaction of the amyloid imaging tracer FDDNP with hallmark Alzheimer's disease pathologies. *J Neurochem.* 2009;109:623–630.

4. Villemagne VL, Furumoto S, Fodero-Tavoletti M, et al. The challenges of tau imaging. *Future Neurol.* 2012;7:409–421.
5. Baskin A, Giannakopoulos P, Ratib O, et al. PET radiotracers for molecular imaging in dementia. *Curr Radiopharm.* 2013;6:215–230.
6. Chien DT, Bahri S, Szardenings AK, et al. Early clinical PET imaging results with the novel PHF-tau radioligand [F-18]-T807. *J Alzheimers Dis.* 2013;34: 457–468.
7. Ballatore C, Smith AB III, Lee VM, et al. Aminothienopyridazines as imaging probes of tau pathology: a patent evaluation of WO2013090497. *Expert Opin Ther Pat.* 2014;24:355–360.
8. Chien DT, Szardenings AK, Bahri S, et al. Early clinical PET imaging results with the novel PHF-tau radioligand [F-18]-T808. *J Alzheimers Dis.* 2014;38: 171–184.
9. Fodero-Tavoletti MT, Furumoto S, Taylor L, et al. Assessing THK523 selectivity for tau deposits in Alzheimer's disease and non Alzheimer's disease tauopathies. *Alzheimers Res Ther.* 2014;6:11.
10. Okamura N, Furumoto S, Fodero-Tavoletti MT, et al. Non-invasive assessment of Alzheimer's disease neurofibrillary pathology using ^{18}F-THK5105 PET. *Brain.* 2014;137:1762–1771.
11. Maruyama M, Shimada H, Suhara T, et al. Imaging of tau pathology in a tauopathy mouse model and in Alzheimer patients compared to normal controls. *Neuron.* 2013;79:1094–1108.
12. Wood H. Alzheimer disease: [^{11}C]PBB3—a new PET ligand that identifies tau pathology in the brains of patients with AD. *Nat Rev Neurol.* 2013;9:599.
13. Waldeck DH. Photoisomerization dynamics of stilbene. *Chem Rev.* 1991;91: 415–436.
14. Fukumura T, Suzuki H, Mukai K, et al. Development of versatile synthesis equipment for multiple production of PET radiopharmaceuticals [abstract]. *J Labelled Comp Radiopharm.* 2007;50(suppl 1):S202.
15. Chen JJ, Huang SJ, Finn RD, et al. Quality control procedure for 6-[^{18}F]fluoro-L-DOPA: a presynaptic PET imaging ligand for brain dopamine neurons. *J Nucl Med.* 1989;30:1249–1256.
16. Yu S. Review of ^{18}F-FDG synthesis and quality control. *Biomed Imaging Interv J.* 2006;2:e57.
17. Jung JC. In-process 20-minute endotoxin "limit test" for positron emission tomography radiopharmaceuticals. *J Am Pharm Assoc.* 2006;46:89–92.
18. Channing MA. Analysis of residual solvents in 2-[^{18}F]FDG by GC. *Nucl Med Biol.* 2001;28:469–471.
19. Takei M, Kida T, Suzuki K. Sensitive measurement of positron emitters eluted from HPLC. *Appl Radiat Isot.* 2001;55:229–234.
20. Wilson AA, Garcia A, Chestakova A, et al. A rapid one-step radiosynthesis of the β-amyloid imaging radiotracer *N*-methyl-[^{11}C]2-(4′-methylaminophenyl)-6-hydroxybenzothiazole ([^{11}C]-6-OH-BTA-1). *J Labelled Comp Radiopharm.* 2004;47:679–682.
21. Andersson JD, Varnas K, Cselenyi Z, et al. Radiosynthesis of the candidate β-amyloid radioligand [^{11}C]AZD2184: positron emission tomography examination and metabolite analysis in cynomolgus monkeys. *Synapse.* 2010;64:733–741.
22. Scheinin NM, Tolvanen TK, Wilson IA, et al. Biodistribution and radiation dosimetry of the amyloid imaging agent ^{11}C-PIB in humans. *J Nucl Med.* 2007;48:128–133.
23. Xia CF, Arteaga J, Chen G, et al. [^{18}F]T807, a novel tau positron emission tomography imaging agent for Alzheimer's disease. *Alzheimers Dement.* 2013;9:666–676.